Journal of
Materials Chemistry C

Materials for optical, magnetic and electronic devices

Accepted Manuscript

This article can be cited before page numbers have been issued, to do this please use: J. Yan, X. Xiong, H. Huang, C. Yuan, L. Guo, L. Wang, G. Tan, H. Gong and X. Jing, *J. Mater. Chem. C*, 2025, DOI: 10.1039/D5TC02015H.

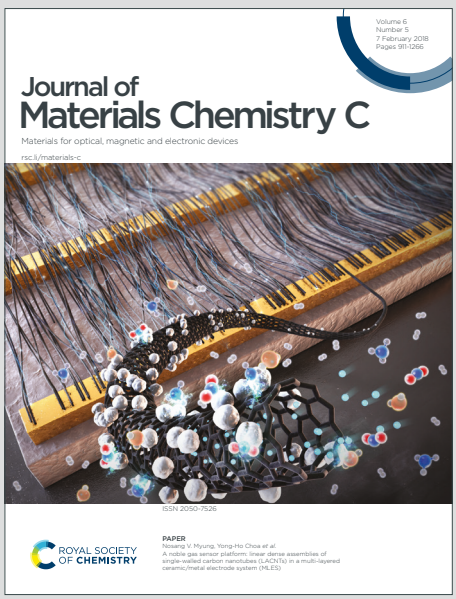

ROYAL SOCIETY OF CHEMISTRY

rsc.li/materials-c

View Article Online
DOI: 10.1039/D5TC02015H

Lanthanum substitution enhanced M-type strontium ferrite absorbing performance based on substitution amount and iron strontium molar ratio

Junjie Yan[a,b], Xiaoqiang Xiong[a,b], Hai Huang[a,b], Chenglong Yuan[a,b], Lanzhou Guo[a,b], Lihong Wang[a,b], Guoguo Tan[a,b], Huayang Gong[a,b], Xiaodong Jing[a,b,c,d,*]

[a] School of Rare earths, University of Science and Technology of China, Hefei, 230026, China

[b] Ganjiang Innovation Academy, Chinese Academy of Sciences, Ganzhou, 341000, China

[c] Institute of Process Engineering, Chinese Academy of Sciences, Beijing, 100190, China

[d] University of Chinese Academy of Sciences, Beijing, 100049, China

Abstract

The development of high-performance microwave absorption materials with low reflection loss (*RL*) and broad effective absorption bandwidth (EAB) is crucial for advanced electromagnetic applications. In this study, La^{3+}-doped M-type hexagonal strontium ferrites with tailored chemical compositions were synthesized via sol-gel auto-combustion. Four series were systematically investigated: $Sr_{(1-x)}Fe_{12}La_xO_{19}$ (x = 0.05, 0.1, 0.15, 0.2, 0.3), $SrFe_{(12-y)}La_yO_{19}$ (y = 0.05, 0.1, 0.15, 0.2, 0.3), $SrFe_{12}La_mO_{19}$ (m = 0.05, 0.1, 0.2), and $SrFe_nLa_{0.05}O_{19}$ (n = 11.5, 12, 12.5, 13). The results reveal that La^{3+} doping concentration and Sr/Fe ratio critically influence morphology and grain size, which in turn govern microwave absorption performance. Specifically, lamellar grains exhibit superior absorption properties compared to granular structures, while smaller grain sizes enhance electromagnetic attenuation. The optimized composition, $SrFe_{12.5}La_{0.05}O_{19}$, featuring a sharp lamellar morphology, achieves exceptional performance: a minimum *RL* of -56.51 dB at 1.49 mm thickness and an EAB expected to exceed 5.05 GHz. Notably, specific compositions exhibit distinct advantages: $SrFe_{13}La_{0.05}O_{19}$ exhibits the deepest *RL* (-65.14 dB) with a unique low-frequency matching point at 5.25 GHz, while $SrFe_{11.5}La_{0.05}O_{19}$ demonstrates the broadest full-spectrum EAB (5.05 GHz). These results validate microstructure engineering as a dominant strategy for designing GHz-range microwave absorbers, where coupled chemical substitution and morphological control enabled tailored electromagnetic

View Article Online
DOI: 10.1039/D5TC02015H

functionality.

Key words: Strontium ferrite; Lanthanum substitution; Microwave absorbing properties; Morphology.

1. Introduction

Wireless communication technology stands as a transformative innovation that has significantly advanced modern society by enabling seamless global connectivity[1,2]. However, the electromagnetic radiation and interference generated by this technology have raised significant concerns, as they not only impair the functionality of electronic devices and potentially endanger human health, but also adversely impact the environment[3–5]. These issues have garnered considerable attention from both the scientific community and society at large. Consequently, the development of high-performance microwave-absorbing materials, characterized by low reflection loss (*RL*) and a broad effective absorption bandwidth (EAB), has become a critical area of research to mitigate these adverse effects[6–8].

M-type hexagonal ferrites have garnered significant research interest as promising microwave-absorbing materials in the gigahertz (GHz) range, particularly 2~18 GHz. This interest stems from their tunable coercivity, high saturation magnetization, strong magnetocrystalline anisotropy, and exceptional chemical stability.[9]. M-type hexagonal ferrites have garnered significant research interest as promising microwave-absorbing materials in the gigahertz (GHz) range, particularly 2~18 GHz. This interest stems from their tunable coercivity, high saturation magnetization, strong magnetocrystalline anisotropy, and exceptional chemical stability.

Nevertheless, their intrinsic natural resonance frequency predominantly resides in the millimeter-wave regime (typically around 45 GHz), restricting their direct utilization in lower-frequency applications[10,11]. To address these limitations, extensive research has focused on modifying their internal magnetic properties through ion substitution strategies[12–15].

The introduction of high-valence cations has proven effective in reducing magnetocrystalline anisotropy and shifting resonance frequencies to lower ranges[16,17]. This substitution mechanism promotes the partial reduction of Fe^{3+} to Fe^{2+}, induces

dual natural resonance behavior, enhances interfacial polarization via elevated dipole density, and activates synergistic electromagnetic loss mechanisms (conductive and polarization losses), thereby significantly expanding the EAB[18,19]. Additionally, rare earth element substitution at the Sr (Ba) sites capitalizes on the distinctive 4f electron configurations of these ions, which refine charge distribution and local crystal field symmetry[20–22]. This optimization not only improves impedance matching but also enhances microwave attenuation efficiency, enabling tailored absorption performance across targeted frequency bands.

Extensive research has been conducted on La^{3+}-substituted hexagonal ferrites[23,24], owing to the compatibility of La^{3+} ions with Sr^{2+} ionic radius, coupled with the valence mismatch-induced charge compensation mechanisms (Fe^{2+} or oxygen defect generation). Liu et al.[25] systematically investigated this system by fabricating $Sr_{(1-x)}Fe_{12}La_xO_{19}$ ($0 \le x \le 0.3$) via sol-gel auto-combustion synthesis. The material retained a single-phase M-type hexagonal structure with platelet-like morphology up to $x = 0.2$. The optimal microwave absorption performance was observed for the $x = 0.1$ composition, exhibiting a *RL* of -22.8 dB at 15.2 GHz (6 mm thickness) and an EAB spanning 14.3~16.1 GHz. Notably, contrary to the theoretical expectation that Fe^{3+} to Fe^{2+} reduction driven by La^{3+} substitution would enhance electromagnetic loss via increased electron hopping and polarization, the absorption performance degraded significantly at higher doping levels ($x \ge 0.15$). A comparable performance degradation trend was documented in our prior studies on rare-earth-doped ferrite systems[26]. This deviation suggests there are some other potential limitations, which may disrupt impedance matching and attenuate synergistic dielectric-magnetic loss processes.

Building upon the aforementioned findings, this study systematically investigates the potentially critical factors governing microwave absorption performance in La^{3+}-doped strontium ferrites. Four series were examined (1) La^{3+} substitution with Sr deficiency $Sr_{(1-x)}Fe_{12}La_xO_{19}$ ($x = 0.05, 0.1, 0.15, 0.2, 0.3$) (2) La^{3+} substitution with Fe deficiency $SrFe_{(12-y)}La_yO_{19}$ ($y = 0.05, 0.1, 0.15, 0.2, 0.3$), (3) La^{3+} doping under fixed stoichiometric ratios $SrFe_{12}La_mO_{19}$ ($m = 0.05, 0.1, 0.2$), and (4) Sr/Fe ratio optimization at constant La^{3+} doping levels $SrFe_nLa_{0.05}O_{19}$ ($n = 11.5, 12, 12.5, 13$). The oxygen

stoichiometry is assumed to remain theoretically ideal throughout the doping process, without deviation from the nominal composition

Comprehensive microstructure characterization revealed that grain morphology evolution (lamellar to granular) and size refinement directly correlate with enhanced electromagnetic attenuation. These microstructural modifications critically influence interfacial polarization dynamics and grain boundary density, thereby governing impedance matching and multi-scale loss mechanisms. The optimal composition, $SrFe_{12.5}La_{0.05}O_{19}$, demonstrated exceptional microwave absorption performance: a minimum *RL* of -56.51 dB at 1.49 mm thickness, with an EAB over 5.06 GHz. This result highlights the efficacy of coupled chemical-microstructural engineering.

2. Experimental

2.1. Raw materials

All chemical reagents used in the experiment were of analytical without other treatment and are listed in Table 1. Deionized water was prepared by an Ultra-pure water system.

Table 1 Chemical reagents used in the experiment

Reagent name	Chemical formula	Purity	Manufacture
Iron nitrate	$Fe(NO_3)_3•9H_2O$	98.5~101.0%	Xilong science
Strontium nitrate	$Sr(NO_3)_2$	≥99.5%	Xilong science
Lanthanum nitrate	$La(NO_3)_3•6H_2O$	99%	Macklin
Citric acid	$C_6H_8O_7•H_2O$	≥99.5%	Xilong science
Ammonia	$NH_3•H_2O$	25%	Xilong science

2.2. Materials synthesis

In this experiment, La^{3+} doped M-type hexagonal ferrites with the compositions $Sr_{(1-x)}Fe_{12}La_xO_{19}$ (x = 0.05, 0.1, 0.15, 0.2, 0.3), $SrFe_{(12-y)}La_yO_{19}$ (y = 0.05, 0.1, 0.15, 0.2, 0.3), $SrFe_{12}La_mO_{19}$ (m = 0.05, 0.1, 0.2) and $SrFe_nLa_{0.05}O_{19}$ (n = 11.5, 12, 12.5, 13) were synthesized via the sol-gel auto-combustion method. Initially, stoichiometric quantities of iron nitrate, strontium nitrate, and lanthanum nitrate were dissolved in 600 mL of deionized water. Citric acid was subsequently added to the metal nitrate solution at a

1:1 molar ratio relative to the total metal ions, and the mixture was magnetically stirred for over 3 h. Upon stabilization of the sol, the pH was adjusted to 7 by the dropwise addition of ammonium hydroxide. The resulting solution was then heated in an oil bath at 90 °C for 24 h to form a viscous liquid, which was further dried in an air oven at 100 °C for over 24 h to obtain the dry gel. Finally, the dry gel was calcined in auto-combustion mode within an electric furnace to remove organic components, yielding a fluffy bulk powder. To achieve optimal phase purity and crystallinity of the synthesized hexagonal phase, the powder was subjected to thermal treatment at 1250 °C for 5 hours in a muffle furnace under ambient atmospheric conditions. The temperature was increased from ambient temperature to 1250 °C at a heating rate of 5 °C/min. A schematic of the fabrication process is presented in Fig. 1.

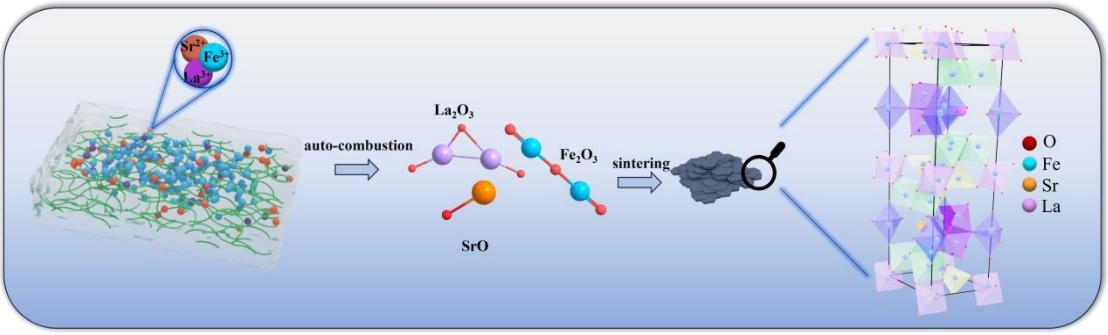

Fig. 1 Schematic of the fabrication process.

2.3. Characterization

The crystal structures and phase compositions of the materials were characterized using an X-ray powder diffractometer (D8 Advance, BRUKER) equipped with Cu-Kα radiation (λ = 0.154 nm). XRD patterns were recorded over a 2θ range of 25°~75°. X-ray photoelectron spectroscopy (XPS, Thermo Scientific K-Alpha) was employed to determine the valence states of the constituent elements, with measurements conducted under ultra-high vacuum conditions at pressures below 10^{-7} Pa. The microscopic morphology of the samples was examined by field emission scanning electron microscopy (FE-SEM, TESCAN Clara) combined with energy-dispersive spectrum (EDS), which was utilized to identify distinct phases and analyze the elemental composition of the surface. Magnetic hysteresis loops were measured at 300 K using a vibrating sample magnetometer (VSM, VersaLab, Quantum Design). The complex

electromagnetic parameters were characterized using a vector network analyzer (VNA, Agilent N5222A) operating in the microwave frequency range of 2~18 GHz. The scattering parameters were systematically recorded using the standard transmission-reflection coaxial line method for subsequent calculation of the complex permittivity and permeability.

3. Result and discussion

3.1. Structural analysis

Fig. 2(a~d) displays the XRD patterns of $Sr_{(1-x)}Fe_{12}La_xO_{19}$, $SrFe_{(12-y)}La_yO_{19}$, $SrFe_{12}La_mO_{19}$ and $SrFe_nLa_{0.05}O_{19}$. The characteristic Bragg reflections observed at 2θ values of 30.4°, 32.3°, 34.2°, 37.2°, 40.4°, 55.2°, 56.9°, and 63.2° correspond to the (110), (107), (114), (203), (205), (217), (2011), and (220) crystallographic planes, respectively, consistent with the standard hexagonal structure of $SrFe_{12}O_{19}$ (space group $P6_3/mmc$)[27]. These results confirm the successful synthesis of strontium ferrites through the sol-gel auto-combustion process.

The structural characterization reveals that the $Sr_{(1-x)}Fe_{12}La_xO_{19}$ series maintains excellent phase purity even at elevated doping concentrations. In the $SrFe_{(12-y)}La_yO_{19}$ series, although a secondary phase of $(Sr_{1-s}La_s)FeO_{3-q}$ emerges at doping levels exceeding $y \geq 0.1$, the characteristic diffraction peaks of this secondary phase remain relatively weak. Notably, the intensity of these $(Sr_{1-s}La_s)FeO_{3-q}$ peaks shows minimal variation with increasing La^{3+} doping concentrations, remaining consistently weak throughout the doping range. Trace amounts of Fe_2O_3 were detected in the $SrFe_nLa_{0.05}O_{19}$ series at n = 13, and minor quantities of a perovskite-type phase $(Sr_{1-s}La_s)FeO_{3-q}$ were observed in the $SrFe_{12}La_mO_{19}$ series at m=0.2. These structural observations provide compelling evidence for the successful substitution of La^{3+} ions into the hexagonal ferrite lattice sites.

Furthermore, the formation of secondary phases is more pronounced in the $SrFe_{(12-y)}La_yO_{19}$ series compared to the $Sr_{(1-x)}Fe_{12}La_xO_{19}$ series at equivalent La^{3+} doping concentrations. This phenomenon suggests a preferential substitution of La^{3+} ions for Sr^{2+} sites rather than Fe^{3+} sites. This site selectivity can be attributed to the significant differences in ionic radius: La^{3+} (1.061 Å) and Sr^{2+} (1.12 Å) exhibit comparable ionic

sizes, whereas Fe^{3+} (0.65 Å) and Fe^{2+} (0.76 Å) possess substantially smaller radius. The closer match between the ionic radius of La^{3+} and Sr^{2+} facilitates the substitution process, as the incorporation of La^{3+} into the Sr^{2+} sites induces less lattice distortion compared to its potential incorporation into the significantly smaller Fe^{3+} sites[23,28].

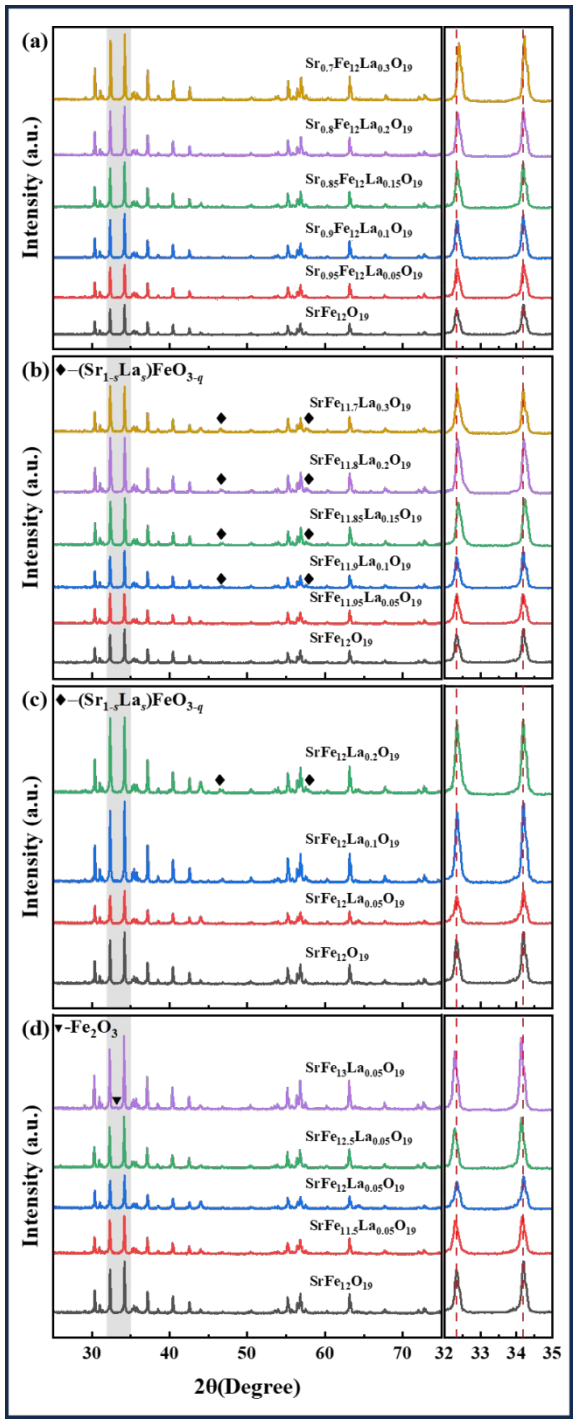

Fig. 2 XRD patterns of (a) $Sr_{(1-x)}Fe_{12}La_xO_{19}$, (b) $SrFe_{(12-y)}La_yO_{19}$, (c) $SrFe_{12}La_mO_{19}$, and (d) $SrFe_nLa_{0.05}O_{19}$ (The right image is a partial enlargement).

Although the radius of La^{3+} is comparable to Sr^{2+}, it is slightly smaller. This

difference in ionic radius can induce internal lattice stress, leading to variations in lattice constants[27]. Fig. 2 illustrates the peak positions within the 2θ range of 32°~35°. For the $Sr_{(1-x)}Fe_{12}La_xO_{19}$ and $SrFe_{(12-y)}La_yO_{19}$ systems, the peaks shift to higher angles when x, $y \geq 0.15$, which indicate a decrease in the lattice constants[29]. While no significant shift is observed for the $SrFe_{12}La_mO_{19}$ system even at the highest doping concentration of $m = 0.2$, suggesting that the maximum solubility limit of La in this system lies within the range of $0.1 < m < 0.2$, as indicated by the presence of secondary peaks in XRD patterns and a secondary phase in SEM images. In the $SrFe_nLa_{0.05}O_{19}$ series, all compositions exhibit peak shifts to lower angles except for $SrFe_{12}La_{0.05}O_{19}$, which maintains a stoichiometric Sr/Fe ratio of 1:12 without deviation. These observed peak shifts provide strong evidence for the successful incorporation of La^{3+} into the crystal lattice.

The lattice parameters of the synthesized samples, including lattice constants (a and c), c/a ratio and unit cell volume (V), are summarized in Table 2. The evolution of lattice parameters c and V with La^{3+} doping concentration is presented in Fig 3, demonstrating good consistency with the XRD pattern analysis shown in Fig. 2. For dynamic La^{3+} doping concentration systems ($Sr_{(1-x)}Fe_{12}La_xO_{19}$, $SrFe_{(12-y)}La_yO_{19}$ and $SrFe_{12}La_mO_{19}$), the a-axis parameter exhibits minor fluctuations and remains relatively constant with increasing in La^{3+} doping concentrations, while the c-axis parameter and unit cell volume show a gradual decrease with higher La^{3+} doping concentrations. This structural contraction can be attributed to the substitution of larger Sr^{2+} ions (1.12 Å) by smaller La^{3+} ions (1.061 Å), leading to reduced interlayer spacing along the c-axis[30]. Similarly, in the $SrFe_nLa_{0.05}O_{19}$ system, the a-axis maintains stability, whereas the c-axis and unit cell volume demonstrate a monotonic decrease as the Sr/Fe ratio deviates from stoichiometry (1:12). This behavior suggests that both La^{3+} doping and Sr/Fe ratio modifications primarily affect the hexagonal structure's vertical stacking rather than basal plane dimensions. The c/a ratios of the synthesized samples, ranging from 3.9116 to 3.9214, provide additional evidence for the formation of M-type hexaferrite structure[31].

View Article Online
DOI: 10.1039/D5TC02015H

Table 2 Lattice parameters (*a*, *c*, and *c*/*a* ratio) and cell volume *V* of the samples

Sample		*a*(Å)	*c*(Å)	*c*/*a*	*V*(Å^3)
$SrFe_{12}O_{19}$		5.8845	23.0612	3.9190	691.57
$Sr_{(1-x)}Fe_{12}La_xO_{19}$	0.05	5.8828	23.0518	3.9185	690.88
	0.1	5.8834	23.0440	3.9168	690.77
	0.15	5.8833	23.0318	3.9148	690.39
	0.2	5.8842	23.0318	3.9142	690.6
	0.3	5.8829	23.0115	3.9116	689.69
$SrFe_{(12-y)}La_yO_{19}$	0.05	5.8829	23.0636	3.9204	691.27
	0.1	5.8820	23.0554	3.9196	690.81
	0.15	5.8822	23.0481	3.9183	690.63
	0.2	5.8831	23.0503	3.9180	690.91
	0.3	5.8822	23.0440	3.9176	690.51
$SrFe_{12}La_mO_{19}$	0.05	5.8856	23.0764	3.9208	692.29
	0.1	5.8830	23.0568	3.9192	691.07
	0.2	5.8826	23.0531	3.9188	690.88
$SrFe_nLa_{0.05}O_{19}$	11.5	5.8832	23.070	3.9214	691.51
	12	5.8856	23.076	3.9208	692.29
	12.5	5.8821	23.065	3.9212	691.1
	13	5.8825	23.050	3.9185	690.76

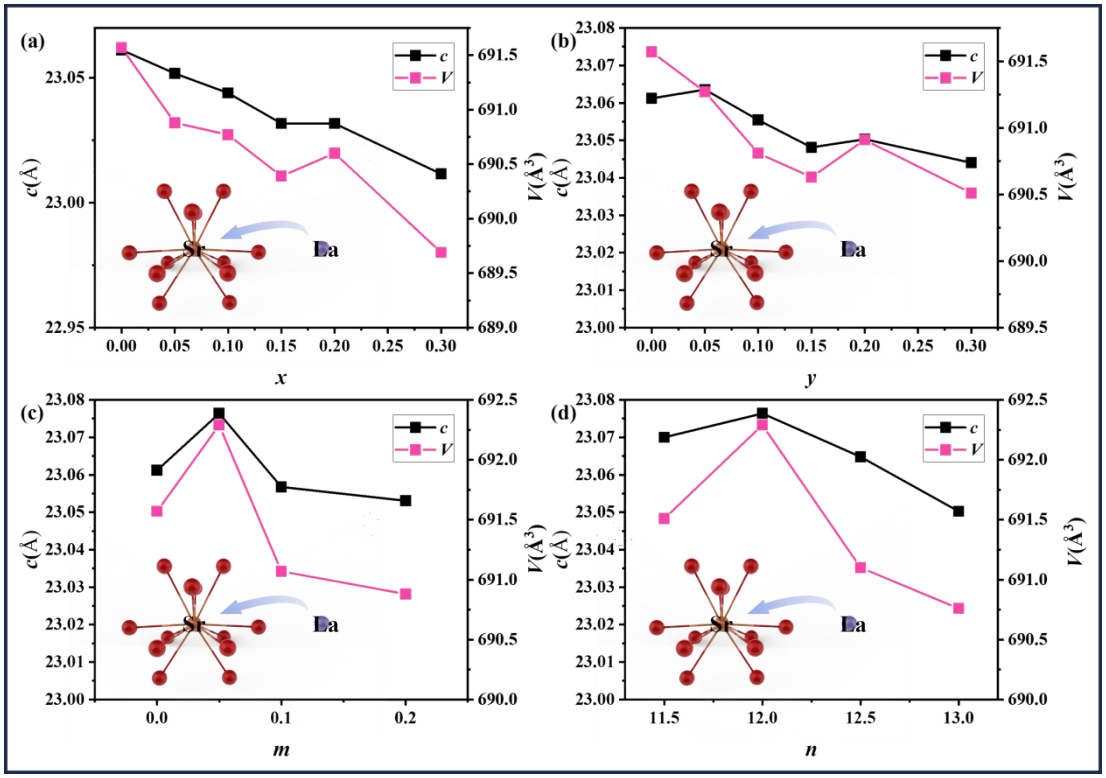

Fig. 3. Lattice parameters *c* and *V* of the samples (a) $Sr_{(1-x)}Fe_{12}La_xO_{19}$, (b) $SrFe_{(12-y)}La_yO_{19}$, (c) $SrFe_{12}La_mO_{19}$, and (d) $SrFe_nLa_{0.05}O_{19}$.

View Article Online
DOI: 10.1039/D5TC02015H

3.2. XPS analysis

X-ray photoelectron spectroscopy (XPS) was employed to investigate the chemical states and elemental composition of the synthesized nanomaterials. Fig. 4 presents the full survey spectra and high-resolution O 1s/Fe 2p spectra for representative samples from the $Sr_{(1-x)}Fe_{12}La_xO_{19}$ and $SrFe_{(12-y)}La_yO_{19}$ series. All spectra were calibrated using the C 1s peak at 284.8 eV as an internal reference. The Fe 2p spectrum reveals two characteristic peaks at binding energies of 710.0 eV (Fe $2p_{3/2}$) and 723.5 eV (Fe $2p_{1/2}$), which can be deconvoluted into multiple components corresponding to Fe^{2+} (709.3 eV and 723.1 eV), Fe^{3+} (710.5 eV and 724.7 eV), and satellite peaks (712.5 eV)[32]. The partial reduction of Fe^{3+} to Fe^{2+} is attributed to charge compensation mechanisms induced by La^{3+} substitution at Sr^{2+} sites, primarily through oxygen vacancy formation rather than cation vacancies[33]. The O 1s spectrum was resolved into three distinct components: lattice oxygen (O_l) at approximately 529 eV, oxygen vacancies (O_d) at 531 eV, and surface-adsorbed oxygen species (O_a) at 533 eV[34]. Comparative analysis revealed that $SrFe_{11.9}La_{0.1}O_{19}$ exhibits a highest oxygen vacancies concentration, as evidenced by the larger O_d peak area. These oxygen vacancies induce the formation of additional dipoles within the material, leading to enhanced interfacial polarization and consequently, increased dielectric loss, which is particularly beneficial for microwave absorption applications[35].

Contrary to theoretical predictions that emphasize Fe^{3+}/Fe^{2+} exchange coupling as the dominant mechanism for microwave absorption in dielectric-loss ferrites, experimental results demonstrate an inverse correlation between La^{3+} content and absorption performance in the $Sr_{(1-x)}Fe_{12}La_xO_{19}$ series. This discrepancy suggests the influence of additional factors beyond Fe^{2+}/ Fe^{3+} exchange coupling.

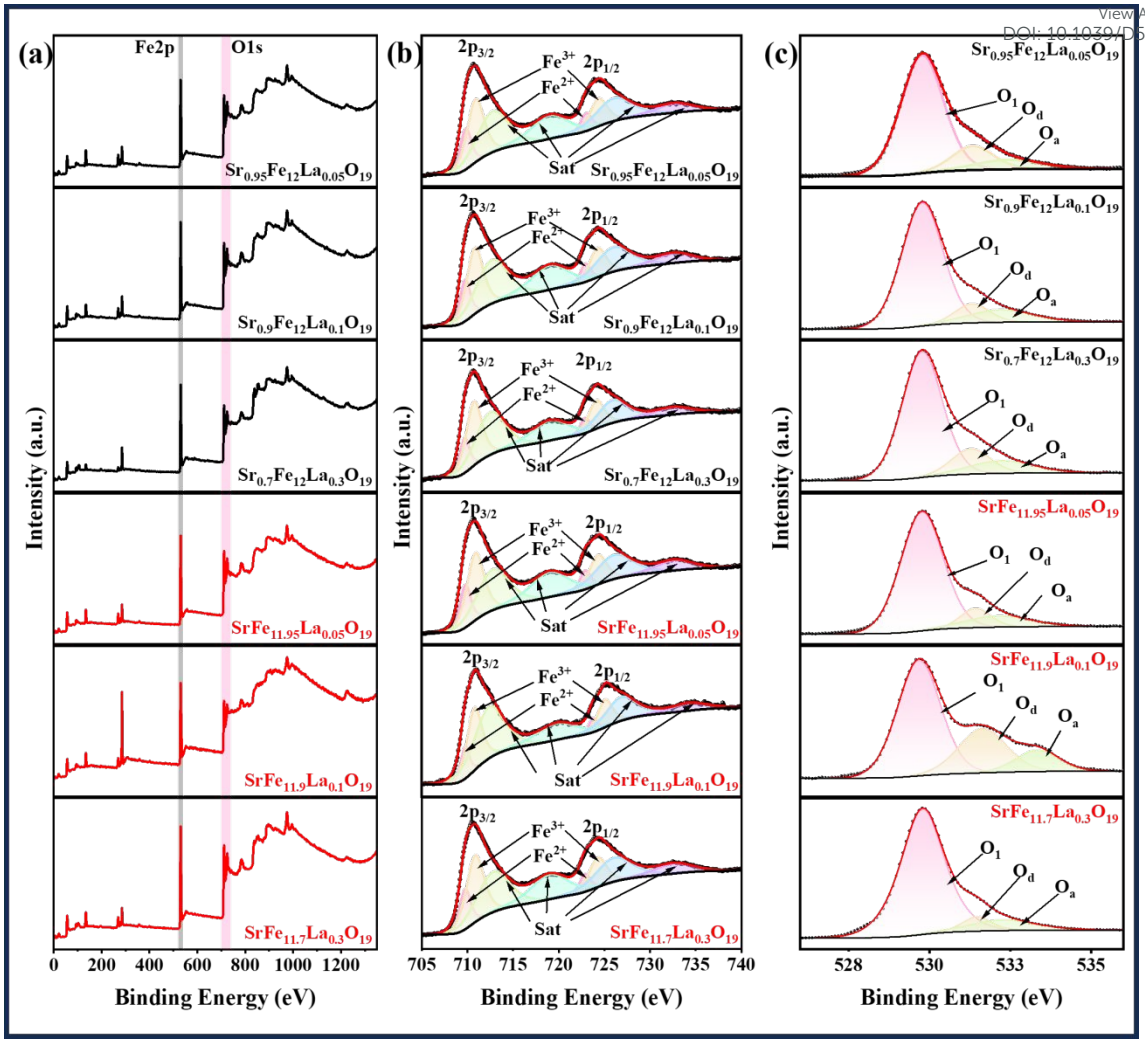

Fig. 4. (a) XPS survey spectra, (b) O1s spectra, and (c) Fe2p spectra of representative samples.

3.3. Morphological and elemental composition analysis

Fig. 5 shows the microstructure and La elemental mapping of the $Sr_{(1-x)}Fe_{12}La_xO_{19}$ series, while Fig. 6 displays the corresponding microstructural evolution in the $SrFe_{(12-y)}La_yO_{19}$ system. All samples display well-defined hexagonal morphologies with high phase purity, except for $SrFe_{11.7}La_{0.3}O_{19}$ (Fig. 6f), which shows trace amounts of secondary phases. In contrast, $Sr_{11.7}Fe_{12}La_{0.3}O_{19}$ maintains high phase purity, as confirmed by both SEM imaging (Fig. 5f) and La elemental mapping via EDS (Fig. 5f'), consistent with the preferential substitution of La^{3+} at Sr^{2+} sites rather than Fe^{3+} sites. This behavior results in superior phase purity and more La^{3+} enter into the lattice for the $Sr_{(1-x)}Fe_{12}La_xO_{19}$ system compared to $SrFe_{(12-y)}La_yO_{19}$.

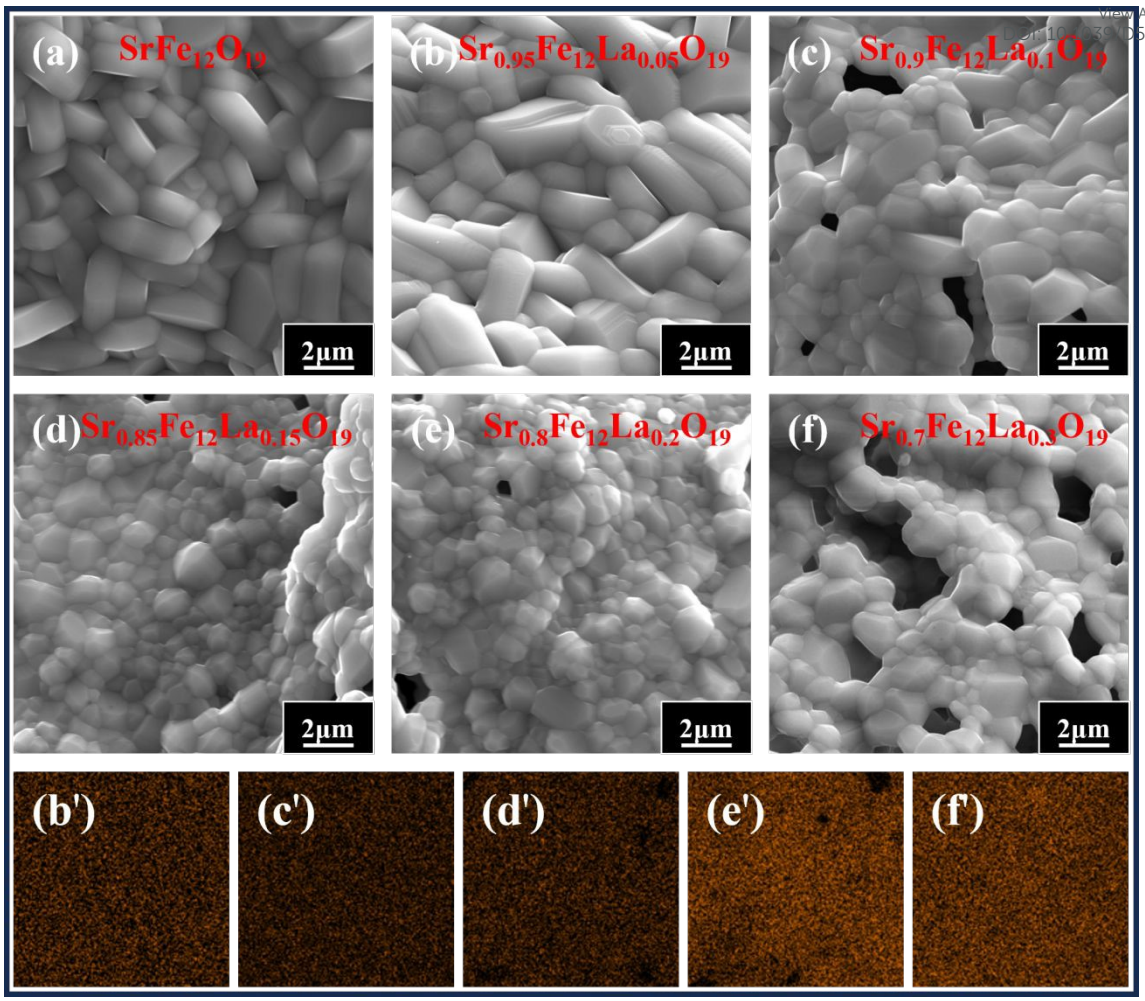

Fig. 5 SEM and EDS images (a) SEM images of $SrFe_{12}O_{19}$, (b~f) SEM images of $Sr_{(1-x)}Fe_{12}La_xO_{19}$, and (b'~f') corresponding La elemental mapping of $Sr_{(1-x)}Fe_{12}La_xO_{19}$.

The comparative analysis reveals significant differences in both phase purity and microstructural characteristics between $Sr_{(1-x)}Fe_{12}La_xO_{19}$ and $SrFe_{(12-y)}La_yO_{19}$ systems. As illustrated in Fig. 5(b), $Sr_{(1-x)}Fe_{12}La_xO_{19}$ initially exhibits a lamellar microstructure at $x = 0.05$. Subsequently, a substantial reduction in grain size and a clear transition to a granular morphology were observed at $x = 0.1$, as illustrated in Fig. 5(c). This morphological transformation stabilizes with further La^{3+} doping ($x \geq 0.15$), as shown in Fig. 5(d)~(f). In contrast, the $SrFe_{(12-y)}La_yO_{19}$ system maintains a predominantly lamellar microstructure throughout the entire doping range ($0.05 \leq y \leq 0.3$), with localized transitions to granular morphology observed only at elevated La^{3+} concentrations ($y \geq 0.15$). At the same time, $SrFe_{(12-y)}La_yO_{19}$ demonstrates a continuous decrease in grain size with higher La^{3+} doping, without any abrupt transitions.

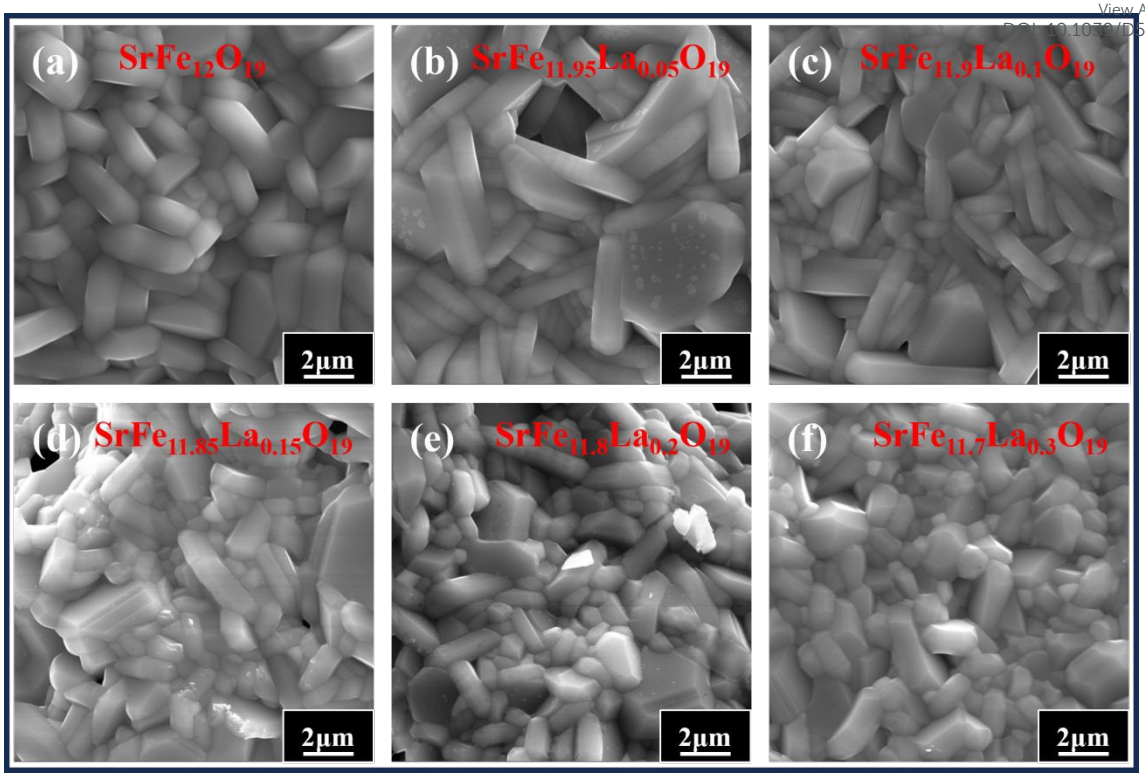

Fig. 6 SEM images (a) $SrFe_{12}O_{19}$, and (b~f) $SrFe_{(12-y)}La_yO_{19}$.

To investigate the factors governing microstructural evolution modulation in La^{3+}-doped M-type ferrites, a series of samples were synthesized with varying La^{3+} concentrations and Sr/Fe ratios. Fig. 7 presents the microstructural characteristics of these samples, highlighting the effects of La^{3+} doping levels (Fig. 7(a)~(c)) and Sr/Fe ratios (Fig. 7(d)~(f)). Notably, the $SrFe_{12}La_mO_{19}$ series (Fig. 7(a)~(c)) demonstrates significant microstructural evolution despite maintaining a constant Sr/Fe ratio, with morphology and grain size strongly dependent on La^{3+} doping levels. Compared to undoped $SrFe_{12}O_{19}$, the lamellar crystals of $SrFe_{12}La_mO_{19}$ exhibit pronounced growth at low La^{3+} concentrations (m = 0.05), as shown in Fig. 7(a). However, with increasing La^{3+} content, the grain size progressively decreases, transitioning to a predominantly granular morphology at m = 0.2, as shown in Fig. 7(c).

Similarly, the $SrFe_nLa_{0.05}O_{19}$ series (Fig. 7(a), (d)~(f)) reveals distinct microstructural characteristics under varying Sr/Fe ratios. At constant La^{3+} doping, the M-phase grain size initially increases slightly while retaining a lamellar microstructure as the Sr/Fe ratio decreases from y = 11.5 to 12.5 (corresponding to Sr/Fe ratios of 0.087, 0.083, and 0.008), as shown in Fig. 7(a), (d), (e). A critical transition occurs at y = 13

(Sr/Fe = 0.077) Fig. 7(f), where a substantial reduction in grain size and a shift to granular morphology are observed.

These findings consistent with the observations for the samples presented in Fig. 5 and Fig. 6. A similar morphological evolution is evident in both the $Sr_{(1-x)}Fe_{12}La_xO_{19}$ and $SrFe_{(12-y)}La_yO_{19}$ series. The maximum grain size and most angular lamellar crystals occur at low La^{3+} doping levels ($x = 0.05$) in both series, as shown in Fig. 5(b) and 6(b). With increasing La^{3+} concentrations, the crystal structure undergoes a gradual transition to granular morphology, accompanied by significant grain refinement in both material systems. In the $Sr_{(1-x)}Fe_{12}La_xO_{19}$ system, a distinct morphological transition occurs at $x = 0.1$ (Fig. 5(c)), corresponding to a Sr/Fe ratio of 0.075. In contrast, the $SrFe_{(12-y)}La_yO_{19}$ system maintains a predominantly lamellar microstructure across the entire doping range ($0.05 \leq y \leq 0.3$), with no significant morphological transitions observed because of minor variations in Sr/Fe ratios (0.084~0.085).

These findings demonstrate that La^{3+} doping concentration and Sr/Fe stoichiometric ratios critically modulate the microstructure and grain size evolution in La^{3+}-doped M-type hexagonal strontium ferrites. Specifically, a Sr/Fe ratio range of 0.075~0.085, combined with low La^{3+} doping levels (≤ 0.01), promotes the formation of lamellar crystal structures. The grain size demonstrated a non-monotonic relationship with both La^{3+} doping concentration and Sr/Fe molar ratio. With increasing La^{3+} substitution, the average grain diameter initially reached a maximum at a doping concentration of 0.05, followed by a subsequent reduction at higher doping levels. Similarly, deviations from the stoichiometric Sr/Fe ratio of 1:12 ($SrFe_{12}O_{19}$) resulted in systematic grain refinement. These optimized microstructural configurations are strongly correlated with enhanced microwave absorption performance, as evidenced by subsequent electromagnetic property.

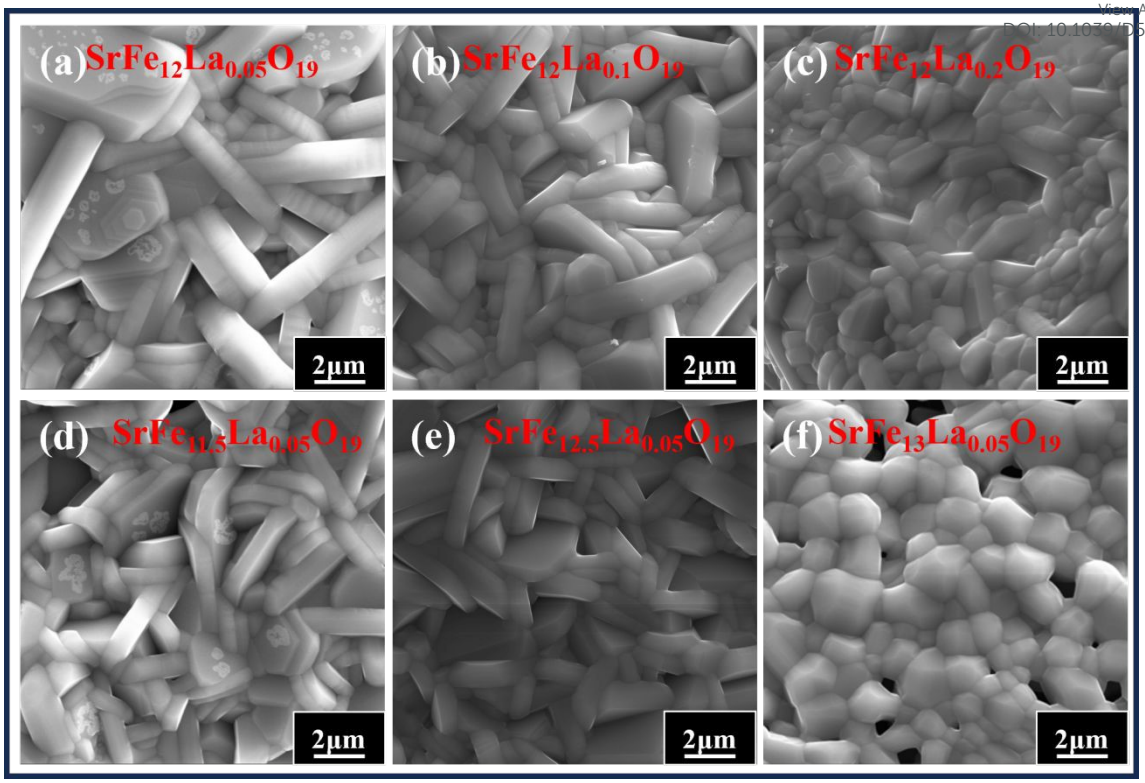

Fig. 7 SEM images of the samples (a~c) $SrFe_{12}La_mO_{19}$, and (d~f) $SrFe_nLa_{0.05}O_{19}$

3.4. Magnetic property analysis

Fig. 8 shows the room-temperature (300 K) magnetic hysteresis loops of $SrFe_{12}O_{19}$, $Sr_{0.95}Fe_{12}La_{0.05}O_{19}$, $Sr_{0.7}Fe_{12}La_{0.3}O_{19}$, $SrFe_{11.95}La_{0.05}O_{19}$ and $SrFe_{11.7}La_{0.3}O_{19}$ under an applied field of 30 kOe. The remanent magnetization (M_r) and coercivity (H_c) were directly extracted from the hysteresis loops, while the saturation magnetization (M_s) was determined according to the law of approach to saturation (LAS)[36]:

$$M = M_s\left(1-\frac{A}{H}-\frac{B}{H^2}\right)-\chi_p H \quad (1)$$

$$B = \frac{4}{15}\frac{K_1^2}{\mu_0^2 M_s^2} \quad (2)$$

where A represents contributions from structural defects and inhomogeneities, B quantifies the magnetocrystalline anisotropy, and χ_p denotes the high-field susceptibility (negligible at 300 K). Thus, Equation (1) simplifies to:

$$M = M_s\left(1-\frac{A}{H}-\frac{B}{H^2}\right) \quad (3)$$

Table 3 summarizes the measured H_c and M_r, along with calculated M_s and squareness ratio (M_r/M_s). The H_c evolution reveals distinct difference between $Sr_{(1-x)}Fe_{12}La_xO_{19}$ and $SrFe_{(12-y)}La_yO_{19}$: $Sr_{(1-x)}Fe_{12}La_xO_{19}$ exhibits a marginal H_c enhancement

at low doping (x = 0.05), whereas $SrFe_{(12-y)}La_yO_{19}$ demonstrates moderate H_c reduction under equivalent doping (y = 0.05). Both systems show significant H_c enhancement at higher substitution levels (x, y = 0.3). This coercivity modulation originates primarily from La^{3+}-induced lattice distortion and defect formation, including cation vacancy pairs and oxygen vacancies. The anomalous H_c reduction in $SrFe_{11.95}La_{0.05}O_{19}$ may be attributed to increased grain size facilitating magnetic domain wall motion[37].

Both series display progressive M_s reduction with increasing La^{3+} concentration, suggesting partial suppression of spin-up magnetic moments. The relatively weak M_s degradation implies that this suppression stems from Fe^{3+} to Fe^{2+} reduction in spin-up sublattices[38]. Importantly, the $Sr_{(1-x)}Fe_{12}La_xO_{19}$ system exhibits significantly slower M_s degradation kinetics compared to $SrFe_{(12-y)}La_yO_{19}$.

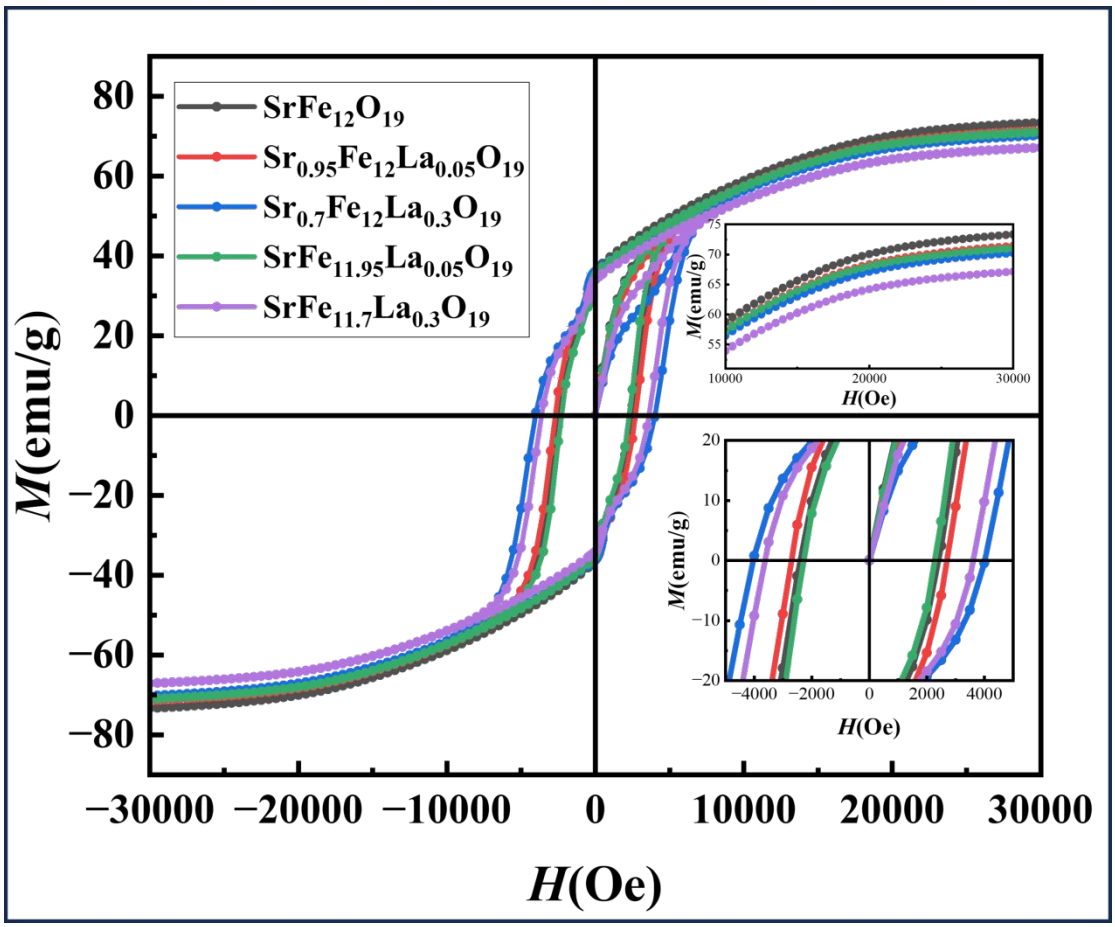

Fig. 8 Hysteresis loops of $SrFe_{12}O_{19}$, $Sr_{0.95}Fe_{12}La_{0.05}O_{19}$, $Sr_{0.7}Fe_{12}La_{0.3}O_{19}$, $SrFe_{11.95}La_{0.05}O_{19}$, and $SrFe_{11.7}La_{0.3}O_{19}$. Enlargement of the near zero field and the saturation magnetic field are shown in the embedded diagram.

View Article Online
DOI: 10.1039/D5TC02015H

Table 3 Values of M_s, M_r, H_c, and M_r/M_s of the samples.

Sample	M_s(emu/g)	M_r (emu/g)	H_c (Oe)	M_r/M_s
$SrFe_{12}O_{19}$	75.92	35.85	2401	0.47
$Sr_{0.95}Fe_{12}La_{0.05}O_{19}$	73.81	35.42	2705	0.48
$Sr_{0.7}Fe_{12}La_{0.3}O_{19}$	72.70	36.12	4037	0.50
$SrFe_{11.95}La_{0.05}O_{19}$	73.40	35.06	2270	0.48
$SrFe_{11.7}La_{0.3}O_{19}$	69.44	34.09	3622	0.49

3.5. Microwave absorption analysis

Owing to the absence of notable magnetic response across 2~18 GHz, magnetic dissipation is negligible in these materials. The primary microwave absorption performance is therefore governed by dielectric loss mechanisms.

The complex permittivity ($\varepsilon_r = \varepsilon' - j\varepsilon''$) quantitatively characterizes the dielectric response of materials to incident electromagnetic radiation and governs the microwave absorption performance of dielectric loss-type absorbers. The real part (ε') of the complex permittivity represents the material's capacity to store electromagnetic energy, while the imaginary part (ε'') reflects its ability to dissipate electromagnetic energy through dielectric losses. The dielectric loss angle ($\tan\delta_e = \varepsilon''/\varepsilon'$) is a critical parameter that quantifies the efficiency of electromagnetic energy conversion into thermal energy per unit volume over time. These three parameters collectively determine the microwave absorption capabilities of dielectric loss-type materials[39-41]. Fig. 9 presents the frequency-dependent behavior of ε' and ε'', as well as the corresponding $\tan\delta_e$, for the $Sr_{(1-x)}Fe_{12}La_xO_{19}$ (Fig. 9(a)~(c)) and $SrFe_{(12-y)}La_yO_{19}$ (Fig. 9(d)~(f)) systems at 2~18 GHz. (Pronounced fluctuations in the electromagnetic parameter profiles arise primarily from the coaxial transmission-line measurement methodology, particularly the utilization of an extended test fixture with a length of approximately 100 mm.)

In the $Sr_{(1-x)}Fe_{12}La_xO_{19}$ system, low-level substitution of La^{3+} ($x = 0.05$) induced a substantial enhancement in the real part of the dielectric constant in the low-frequency range compared to undoped $SrFe_{12}O_{19}$. The ε' and ε'' exhibit frequency-dependent fluctuations with an overall decreasing trend, which displays a typical frequency dispersion behavior[42]. The $\tan\delta_e$ remains relatively stable with no noticeable fluctuations, showing no distinct increasing or decreasing trend, suggesting the presence of multiple dielectric loss mechanisms[43]. A sharp reduction in overall

dielectric loss capability occurs at x = 0.1 with increasing La^{3+} doping concentration, after which the dielectric parameters stabilize within a lower range. This behavior correlates with the microstructural evolution described earlier, where a morphological transition from lamellar to granular microstructure is observed in the $Sr_{(1-x)}Fe_{12}La_xO_{19}$ system at x = 0.1 (Fig. 5(c)). This transition stabilizes with further La^{3+} doping (x = 0.15~0.3), as illustrated in Fig. 5(d)~(f).

A similar trend is observed in the $SrFe_{(12-y)}La_yO_{19}$ system at low La^{3+} doping levels (y = 0.05), where the dielectric parameters exhibit comparable behavior. The ε' and ε'' show a significant increase followed by a decreasing trend, while $\tan\delta_e$ remains relatively stable high values with only minor fluctuations in the 8~16GHz range, indicating consistent dielectric loss behavior across the frequency range.

In contrast to the $Sr_{(1-x)}Fe_{12}La_xO_{19}$ system, the $SrFe_{(12-y)}La_yO_{19}$ system exhibits distinct dielectric behavior with increasing La^{3+} doping. The dielectric parameters rise with La^{3+} concentration, peaking at y = 0.1, after which they decline with a relatively constant value. Notably, both the magnitude and trend of these parameters undergo significant changes. The ε'' and $\tan\delta_e$ display multiple fluctuations or an increasing trend, suggesting the presence of diverse dielectric loss mechanisms[40,41]. The peak values of all dielectric parameters in the $SrFe_{(12-y)}La_yO_{19}$ system surpass those in the $Sr_{(1-x)}Fe_{12}La_xO_{19}$ system. The evolution of dielectric parameters in the $SrFe_{(12-y)}La_yO_{19}$ system with increasing La^{3+} doping aligns with its microstructural evolution. At low La^{3+} concentrations (y = 0.05), the grain size reaches its maximum. At y = 0.1, a reduction in grain size occurs while maintaining a lamellar morphology, coinciding with the peak in dielectric parameters. Further doping (y = 0.15) induces the emergence of granular grains alongside lamellar grains, corresponding to an inflection point in dielectric properties. With continued doping, the proportion of granular grains gradually increases, accompanied by a steady decline in dielectric parameters.

View Article Online
DOI: 10.1039/D5TC02015H

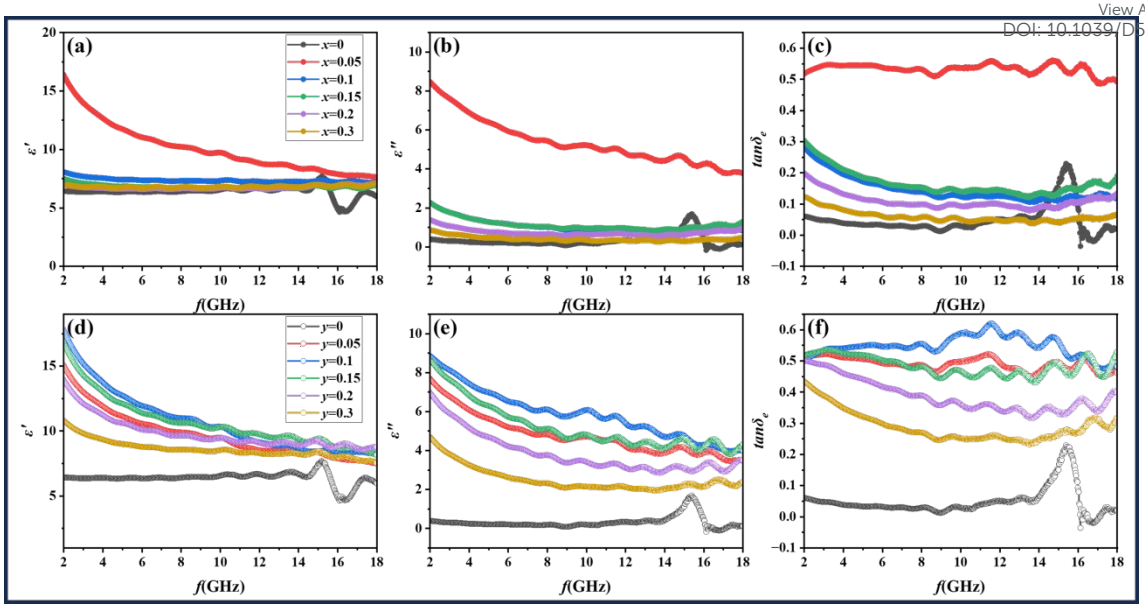

Fig. 9 The dielectric parameters (ε', ε'' and tanδ_e) of the samples (a~c) $Sr_{(1-x)}Fe_{12}La_xO_{19}$, and (d~f) $SrFe_{(12-y)}La_yO_{19}$

Fig. 10 presents the dielectric parameters of two series of samples: $SrFe_{12}La_mO_{19}$ with varying La^{3+} concentrations (Fig. 10(a~c)) and $SrFe_nLa_{0.05}O_{19}$ with varying Sr/Fe stoichiometric ratios (Fig. 10(d~f)). The $SrFe_{12}La_mO_{19}$ system exhibits a pronounced enhancement in dielectric properties at low La^{3+} doping levels (m = 0.05). This improvement is attributed to the incorporation of trace La^{3+} ions, which substitute Sr^{2+} site. The resulting valence mismatch generates defect ion pairs and oxygen vacancies, acting as effective polarization centers[44]. Simultaneously, partial reduction of Fe^{3+} to Fe^{2+} occurs to maintain charge neutrality, with the ensuing Fe^{3+}/Fe^{2+} exchange coupling further amplifying dielectric performance[45]. With increasing La^{3+} concentration, dielectric properties progressively improve, reaching a maximum at m = 0.1. This enhancement arises from the increased density of defect structures (ion pairs and oxygen vacancies) and grain size reduction (Fig. 7b), which enhances interface polarization and promotes multiple reflections[46]. However, beyond m = 0.2, dielectric performance deteriorates concurrently with a microstructural transition in $SrFe_{12}La_{0.2}O_{19}$, characterized by the emergence of granular grains intermingled with lamellar grains. This morphological evolution underscores the critical dependence of dielectric properties on crystal microstructure.

In the $SrFe_nLa_{0.05}O_{19}$ system, the La^{3+} doping concentration remains fixed,

ensuring consistent levels of Fe^{2+} ions. The Sr/Fe ratio is modulated by varying the Fe content, which is demonstrated to critically influence crystal morphology in previous section. The dielectric properties of $SrFe_{11.5}La_{0.05}O_{19}$ and $SrFe_{12}La_{0.05}O_{19}$ are comparable. However, as the Fe proportion increases, the dielectric performance peaks in $SrFe_{12.5}La_{0.05}O_{19}$, where relatively small grain size and lamellar microstructure enhance interfacial polarization and promote multiple electromagnetic wave reflections. A significant deterioration in dielectric properties occurs in $SrFe_{13}La_{0.05}O_{19}$, coinciding with a morphological transition from lamellar to granular grains. This observation suggests superior dielectric performance in lamellar microstructures compared to granular configurations. Mechanistically, the densely packed granular grains with rounded exteriors reduce intergranular spacing and surface area compared to angular lamellar grains. These structural constraints inhibit interfacial polarization and limit electromagnetic wave reflections, ultimately degrading dielectric performance.

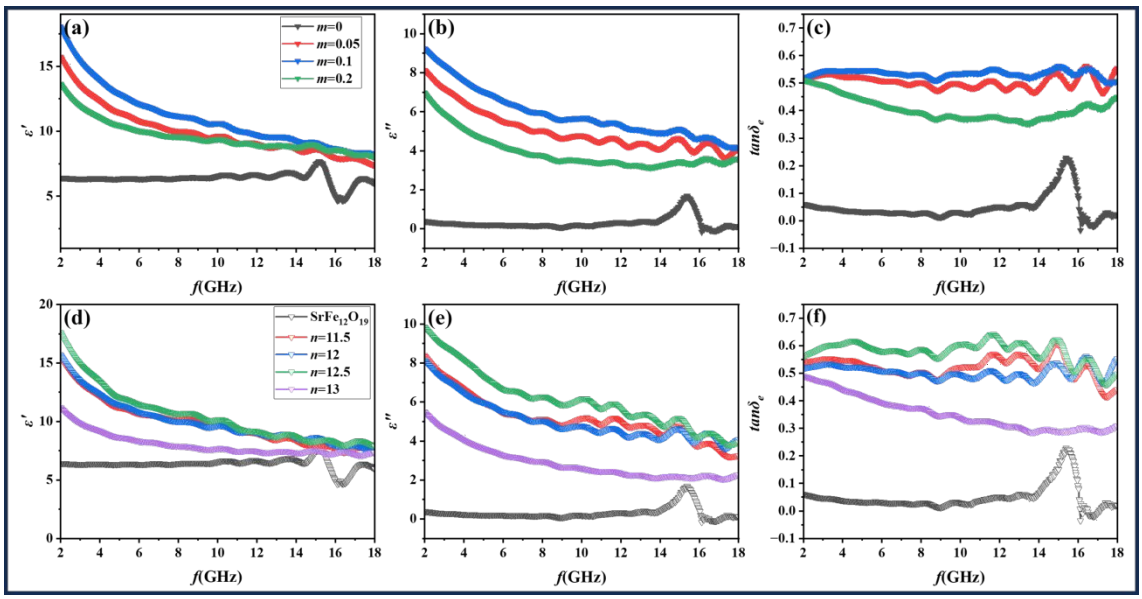

Fig. 10 The dielectric parameters (ε', ε'' and $\tan\delta_e$) of the samples (a~c) $SrFe_{12}La_mO_{19}$, and (d~f) $SrFe_nLa_{0.05}O_{19}$.

Fig. 11 shows the frequency-dependent attenuation coefficient (α) characteristics of the synthesized samples. All compositions exhibit a characteristic monotonic increase in α with frequency, except for the $Sr_{(1-x)}Fe_{12}La_xO_{19}$ series at higher doping levels ($x \geq 0.1$), which maintains consistently low α values across the entire measured frequency range. This anomalous behavior correlates with the evolution of dielectric

parameters, suggesting a common internal ion environmental and microstructural origin. Which enhance interfacial polarization and promote multiple reflections. These results demonstrate that microstructural engineering (grain morphology, defect distribution) dominates over compositional effects in governing GHz-range electromagnetic attenuation.

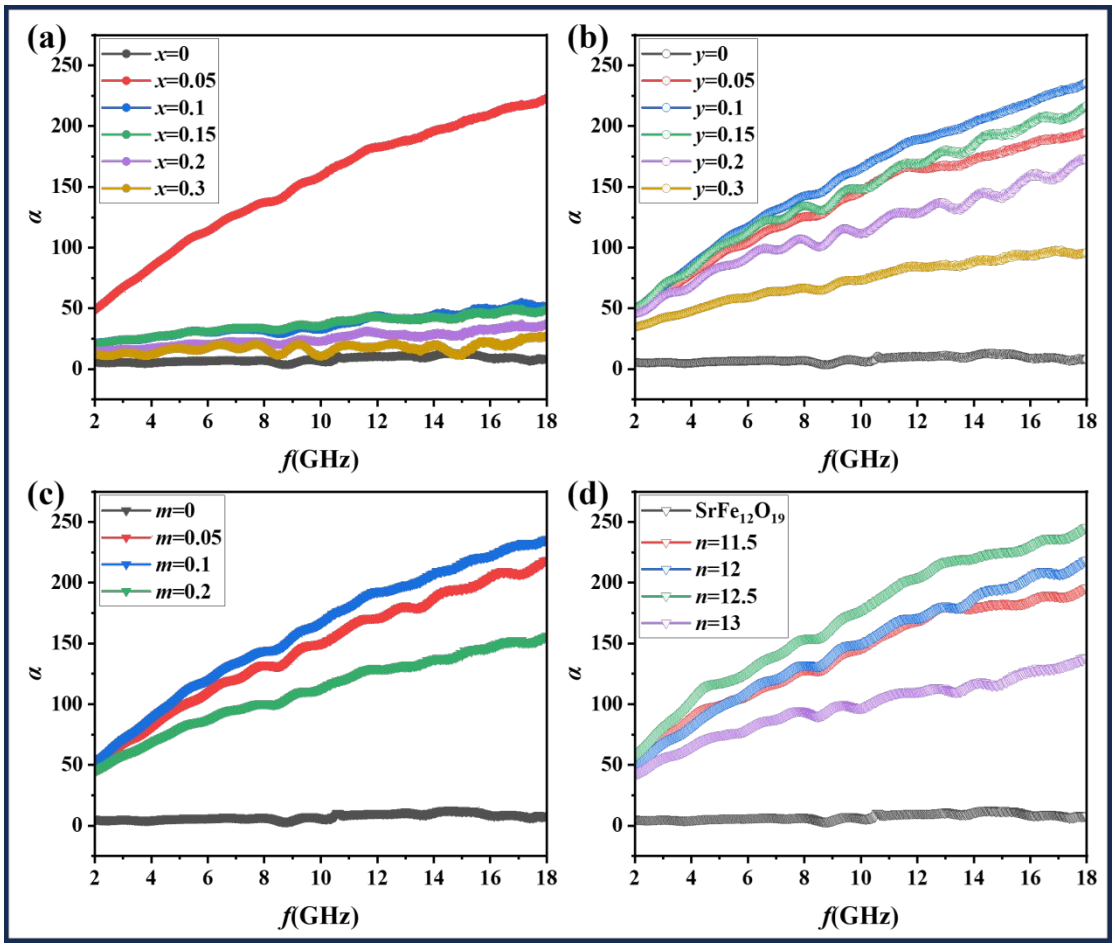

Fig. 11 The attenuation constant of samples (a) $Sr_{(1-x)}Fe_{12}La_xO_{19}$, (b) $SrFe_{(12-y)}La_yO_{19}$, (c) $SrFe_{12}La_mO_{19}$, and (d) $SrFe_nLa_{0.05}O_{19}$

In addition to electromagnetic wave attenuation, impedance matching plays a pivotal role in determining the microwave absorption performance of materials. According to transmission line theory, Z_{in}, RL and Z_r are calculated using the following equations[47-49]:

$$Z_{\text{in}} = Z_0\sqrt{\mu_r/\varepsilon_r}\tanh\left[j\left(\frac{2\pi fd}{c}\right)\mu_r\varepsilon_r\right] \quad (4)$$

$$RL(\text{dB}) = 20\log\left|\frac{(Z_{\text{in}}-Z_0)}{(Z_{\text{in}}+Z_0)}\right| \quad (5)$$

$$Z_r = |Z_{\text{in}}/Z_0| \quad (6)$$

where Z_{in} denotes the input impedance at the air-absorber interface, Z_0 represents the intrinsic impedance of free space. ε_r and μ_r represent the complex relative permittivity and permeability, respectively. The parameter d corresponds to the absorber thickness.

Fig. 12 presents three-dimensional representations of the reflection loss (*RL*) and impedance matching ratio (Z_r) for four optimized samples: (a) $Sr_{0.95}Fe_{12}La_{0.05}O_{19}$ (b) $SrFe_{11.9}La_{0.1}O_{19}$ (c) $SrFe_{12}La_{0.1}O_{19}$ (d) $SrFe_{12.5}La_{0.05}O_{19}$. These samples exhibit superior dielectric properties within their respective systems: $Sr_{(1-x)}Fe_{12}La_xO_{19}$, $SrFe_{(12-y)}La_yO_{19}$, $SrFe_{12}La_mO_{19}$ and $SrFe_nLa_{0.05}O_{19}$. The upper surface, rendered in a blue-yellow gradient, quantifies the reflection loss (*RL*), and the lower surface, depicted in light cyan, corresponds to the impedance matching ratio (Z_r). Critical contour lines are annotated in the 3D models: the -10 dB *RL* contour (threshold for effective absorption) and the Z_r = 1 contour (optimal impedance matching)[50]. A key observation is the precise alignment of the *RL* minima (peaks in absorption) with the Z_r = 1 contour. Furthermore, the effective absorption bandwidth consistently resides near the Z_r = 1 contour, despite the excellent dielectric properties of the samples across the 2~18 GHz frequency range[51]. These findings conclusively demonstrate that optimizing impedance matching is critical for enhancing microwave absorption performance, as it facilitates maximal energy penetration and minimizes reflection at the air-absorber interface.

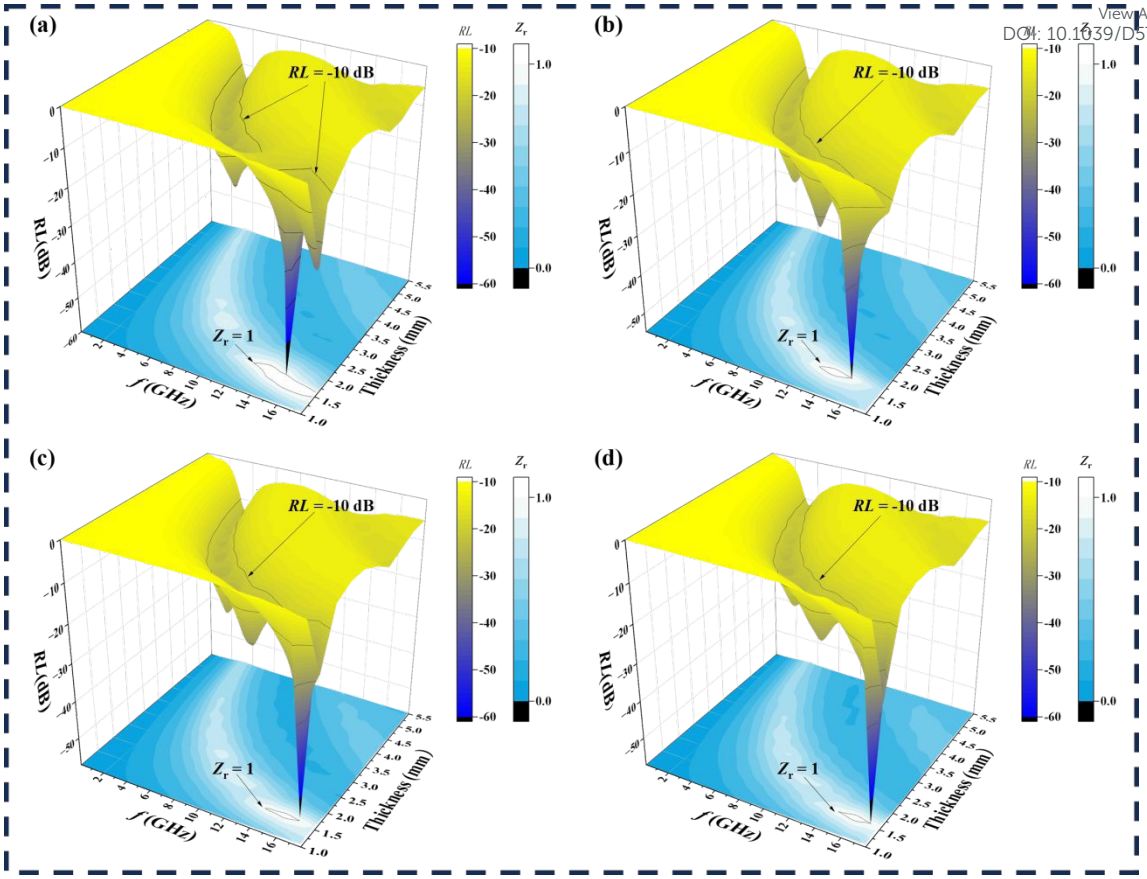

Fig. 12 3D models of reflection loss (*RL*) and impedance matching (Z_r) for the samples (a) $Sr_{0.95}Fe_{12}La_{0.05}O_{19}$, (b) $SrFe_{11.9}La_{0.1}O_{19}$, (c) $SrFe_{12}La_{0.1}O_{19}$, and (d) $SrFe_{12.5}La_{0.05}O_{19}$.

Fig. 13 presents the frequency-dependent (2~18 GHz) *RL* and Z_r for La^{3+}-doped M-type strontium ferrite composites at their respective thickness-optimized configurations. Notably, the frequency corresponding to the minimum reflection loss coincides precisely with the $Z_r = 1$ condition, signifying optimal impedance matching. The results of the minimum reflection loss (*RL*) align with the dielectric properties discussed earlier, where trace amounts of La^{3+} doping enhance dielectric losses in M-type strontium ferrites, thereby improving microwave absorption performance.

For dynamic La^{3+} doping concentration systems ($Sr_{(1-x)}Fe_{12}La_xO_{19}$, $SrFe_{(12-y)}La_yO_{19}$ and $SrFe_{12}La_mO_{19}$), the absorption performance demonstrates progressive enhancement with increasing La^{3+} concentration, revealing distinct transition point in all systems except the $Sr_{(1-x)}Fe_{12}La_xO_{19}$ configuration. In the fixed-concentration system $SrFe_nLa_{0.05}O_{19}$, optimal absorption performance is achieved at the $SrFe_{12.5}La_{0.05}O_{19}$ composition, where the Sr/Fe molar ratio approaching 1:12.5 exhibits better absorption performance.

In the $Sr_{(1-x)}Fe_{12}La_xO_{19}$ system, optimal absorption performance is achieved at x = 0.05 ($Sr_{0.95}Fe_{12}La_{0.05}O_{19}$), demonstrating exceptional performance with a *RL* of -59.44 dB and an EAB of 5.12 GHz at 1.7 mm thickness, coupled with near-ideal impedance matching ($Z_r \approx 1$). The $SrFe_{(12-y)}La_yO_{19}$ system shows competing optimization parameters: while $SrFe_{11.95}La_{0.05}O_{19}$ exhibits the deepest *RL*, $SrFe_{11.9}La_{0.1}O_{19}$ offers superior broadband performance (EAB > 4.56 GHz at 1.61 mm) with extended high-frequency absorption beyond 18 GHz and wider $Z_r \approx 1$ region. Similarly, $SrFe_{12}La_mO_{19}$ peaks at m = 0.1 (*RL* = -55.64 dB, thickness = 1.55 mm), showing particular efficacy in higher frequencies (>18 GHz). Most remarkably, the $SrFe_nLa_{0.05}O_{19}$ system demonstrates that synergistic optimization of both chemical composition and microstructure through Sr/Fe ratio and La^{3+} doping concentration can yield excellent microwave absorption performance. In particular, the $SrFe_{12.5}La_{0.05}O_{19}$ composition exhibits optimal characteristics (RL = -56.51 dB at 1.49 mm).

These findings collectively establish that microwave absorption in hexaferrites is governed by a hierarchical optimization framework involving two interdependent: La^{3+} doping concentration and optimized cation stoichiometry control. The doping process serves as the primary activation mechanism for absorption capability. Both factors synergistically influence the crystallographic microstructure through ionic substitution effects, thereby modulating the electromagnetic wave attenuation characteristics. Fig. 14 illustrates the activation mechanism and performance enhancement mechanisms governing microwave absorption in La^{3+}-doped M-type hexaferrites.

View Article Online
DOI: 10.1039/D5TC02015H

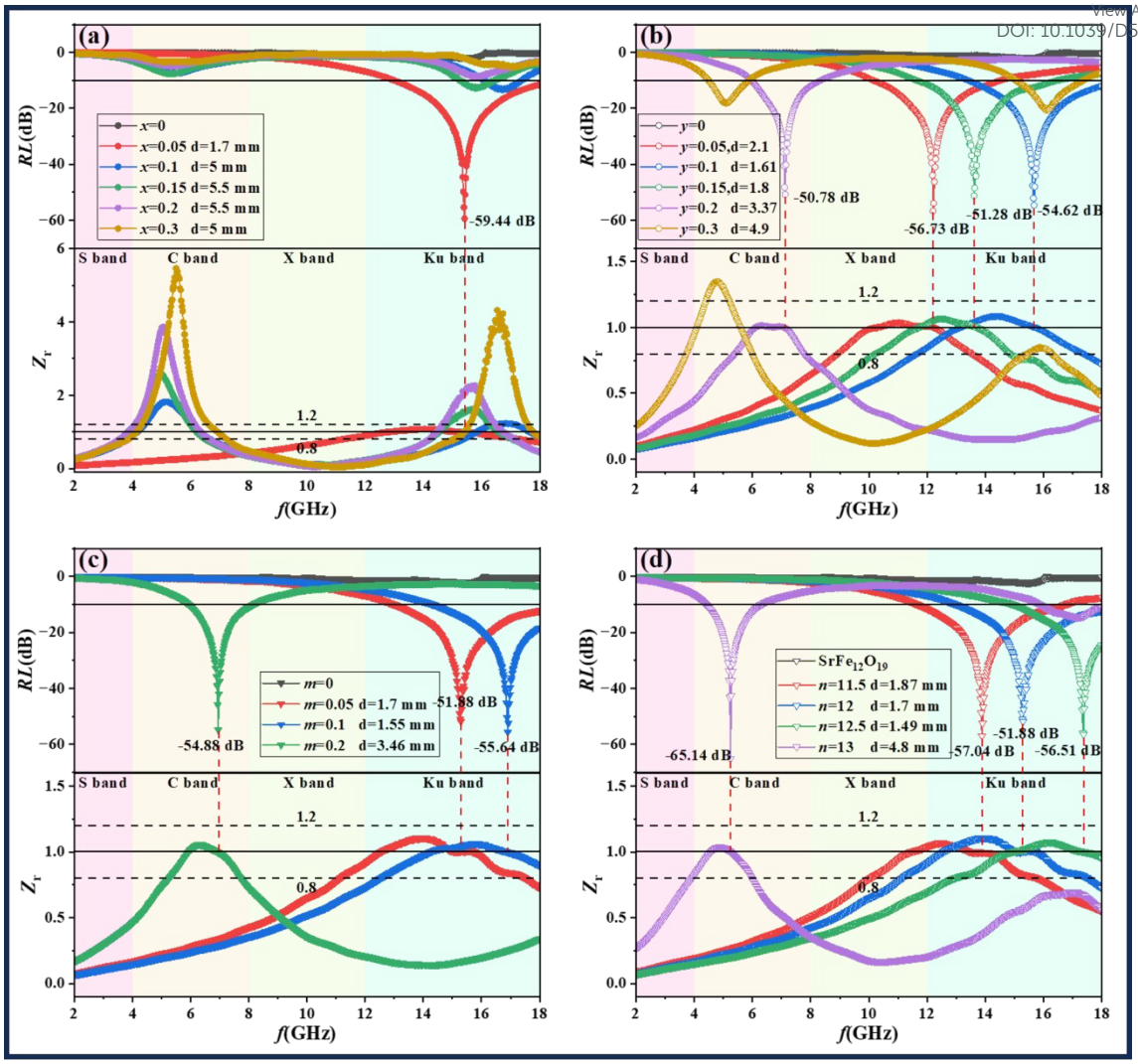

Fig. 13 Frequency dependence of reflection loss and impedance matching for (a) $Sr_{(1-x)}Fe_{12}La_xO_{19}$, (b) $SrFe_{(12-y)}La_yO_{19}$, (c) $SrFe_{12}La_mO_{19}$, and (d) $SrFe_nLa_{0.05}O_{19}$

Table 4 Microwave absorption properties of the samples

Samples		RL_{min}(dB)	Matching frequency(GHz)	Thickness(mm)	EAB(GHz)
$Sr_{(1-x)}Fe_{12}La_xO_{19}$	0.05	-59.44	15.40	1.70	5.01(12.99~18.00)
	0.1	-13.38	16.70	5.00	1.21(16.12~17.33)
	0.15	-12.94	15.81	5.50	1.18(15.25~16.43)
	0.2	-	-	-	-
	0.3	-	-	-	-
$SrFe_{(12-y)}La_yO_{19}$	0.05	-56.73	12.20	2.10	4.34(10.17~14.51)
	0.1	-54.62	15.67	1.61	4.56(13.44~18.00)
	0.15	-51.28	13.61	1.80	4.76(11.67~16.43)
	0.2	-50.78	7.13	3.37	2.33(5.98~8.31)
	0.3	-18.17/ -20.73	5.09/16.1	4.90	1.36(4.51~5.87) /2.28(15.07~17.35)
$SrFe_{12}La_mO_{19}$	0.05	-51.88	15.29	1.70	5.01(12.99~18.00)

	0.1	-55.64	16.90	1.50	3.65(14.35~18.00)
	0.2	-54.88	6.95	3.46	2.19(5.94~8.13)
$SrFe_nLa_{0.05}O_{19}$	11.5	-57.04	13.88	1.87	5.05(11.67~16.72)
	12	-51.88	15.29	1.70	5.01(12.99~18.00)
	12.5	-56.51	17.37	1.49	3.02(14.98~18.00)
	13	-65.14	5.25	4.80	1.88(4.42~6.30)

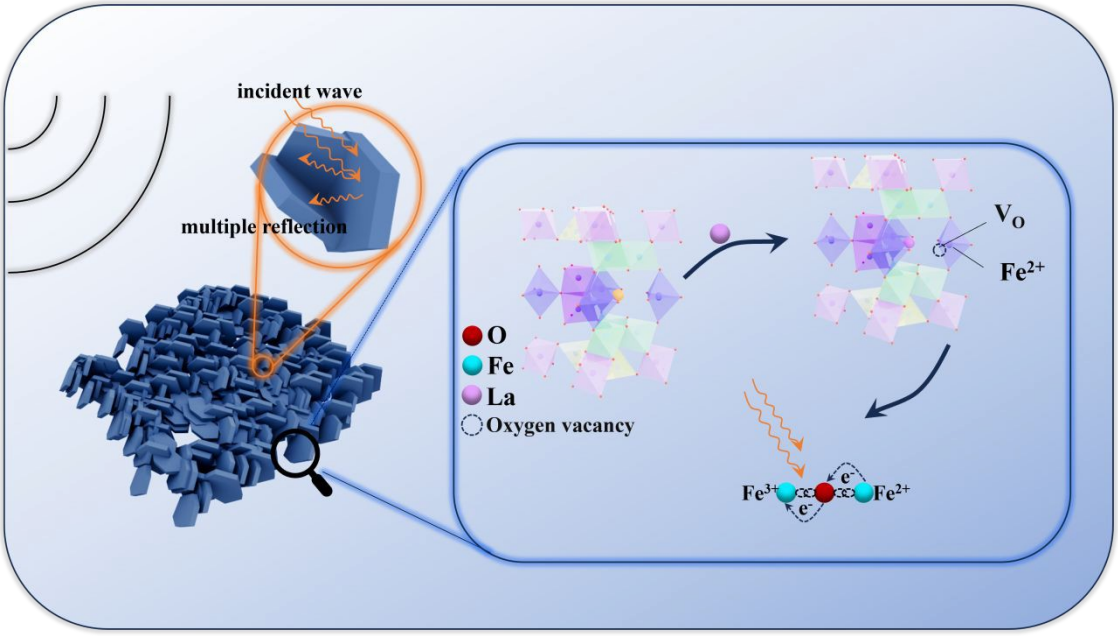

Fig. 14 Activation and enhancement mechanisms governing microwave absorption in La^{3+}-doped M-type hexaferrites.

4. Conclusions

This study systematically investigated La^{3+}-doped M-type hexagonal strontium ferrites synthesized via sol-gel auto-combustion across four compositional series. Key findings reveal that microwave absorption performance is predominantly governed by microstructural evolution rather than La^{3+} doping concentration alone. The doping process functions as the primary activation mechanism for absorption capability, which causes the generation of defect ion pairs and oxygen vacancies, acting as effective polarization centers. Simultaneously, La^{3+} doping concentration synergistically regulates grain morphology and dimensional characteristics in conjunction with Sr/Fe stoichiometric optimization. Notably, the lamellar-structured $SrFr_{12.5}La_{0.05}O_{19}$ achieves exceptional performance: a minimum reflection loss (*RL*) of -56.51 dB at 1.49 mm thickness and an effective absorption bandwidth (EAB) spanning over 5.06 GHz. This enhancement is attributed to two factors: multi-reflection loss facilitated by

View Article Online
DOI: 10.1039/D5TC02015H

interlamellar gaps and interfacial polarization at grain boundaries due to reduced stacking density. These results suggest microstructure modulation as an important strategy for advancing GHz-range microwave absorbers.

Declaration of competing interest

The authors declare that they have no known competing financial interests or personal relationships that could have appeared to influence the work reported in this paper.

Acknowledgments

We gratefully acknowledge the financial support from the grant from the National Key R&D Program of China (No. 2023YFB3809200) and the Research Projects of Ganjiang Innovation Academy, Chinese Academy of Sciences (E355B001).

View Article Online
DOI: 10.1039/D5TC02015H

References

[1] B. Yang, J. Fang, C. Xu, H. Cao, R. Zhang, B. Zhao, M. Huang, X. Wang, H. Lv, R. Che, One-Dimensional Magnetic FeCoNi Alloy Toward Low-Frequency Electromagnetic Wave Absorption, *Nano-Micro Lett*. 14 (2022) 170. https://doi.org/10.1007/s40820-022-00920-7.

[2] D. Lan, M. Qin, J. Liu, G. Wu, Y. Zhang, H. Wu, Novel binary cobalt nickel oxide hollowed-out spheres for electromagnetic absorption applications, *Chem. Eng. J*. 382 (2020) 122797. https://doi.org/10.1016/j.cej.2019.122797.

[3] C.L. Russell, 5 G wireless telecommunications expansion: Public health and environmental implications, *Environ. Res*. 165 (2018) 484–495. https://doi.org/10.1016/j.envres.2018.01.016.

[4] J. Yin, X. Xu, J. Ji, X. Li, X. Cheng, Synthesis and Microwave Absorption Properties of Fe_3O_4 /CuS Composites, *Phys. Status Solidi A*. 219 (2022) 2200189. https://doi.org/10.1002/pssa.202200189.

[5] A. Napp, S. Joosten, D. Stunder, C. Knackstedt, M. Zink, B. Bellmann, N. Marx, P. Schauerte, J. Silny, Electromagnetic Interference With Implantable Cardioverter-Defibrillators at Power Frequency: An In Vivo Study, *Circulation*. 129 (2014) 441–450. https://doi.org/10.1161/CIRCULATIONAHA.113.003081.

[6] M. Zong, Y. Huang, X. Ding, N. Zhang, C. Qu, Y. Wang, One-step hydrothermal synthesis and microwave electromagnetic properties of RGO/$NiFe_2O_4$ composite, *Ceram. Int.* 40 (2014) 6821–6828. https://doi.org/10.1016/j.ceramint.2013.11.145.

[7] H. Lv, Z. Yang, H. Xu, L. Wang, R. Wu, An Electrical Switch-Driven Flexible Electromagnetic Absorber, *Adv. Funct. Mater*. 30 (2020) 1907251. https://doi.org/10.1002/adfm.201907251.

[8] S. Dong, X. Zhang, X. Li, J. Chen, P. Hu, J. Han, SiC whiskers-reduced graphene oxide composites decorated with MnO nanoparticles for tunable microwave absorption, *Chem. Eng. J*. 392 (2020) 123817. https://doi.org/10.1016/j.cej.2019.123817.

[9] J. Li, H. Zhang, V.G. Harris, Y. Liao, Y. Liu, Ni–Ti equiatomic co-substitution of hexagonal M-type $Ba(NiTi)_xFe_{12-2x}O_{19}$ ferrites, *J. Alloys Compd*. 649 (2015) 782–787. https://doi.org/10.1016/j.jallcom.2015.07.173.

[10] F.M.M. Pereira, M.R.P. Santos, R.S.T.M. Sohn, J.S. Almeida, A.M.L. Medeiros, M.M. Costa, A.S.B. Sombra, Magnetic and dielectric properties of the M-type barium strontium hexaferrite ($Ba_xSr_{1-x}Fe_{12}O_{19}$) in the RF and microwave (MW) frequency range, *J. Mater. Sci. Mater. Electron*. 20 (2009) 408–417. https://doi.org/10.1007/s10854-008-9744-8.

[11] Q. Zhao, X. Xiong, X. Yang, Q. Wang, T. Zhao, H. Gong, G. Tan, X. Jing, Mechanism of praseodymium yttrium regulating the absorption properties of M-type strontium ferrite: From single phase to multi phase mixed system, *Mater. Today Chem*. 41 (2024) 102317. https://doi.org/10.1016/j.mtchem.2024.102317.

[12] X. Xiong, X. Jing, Z. Chen, Q. Zhao, Z. Li, X. Yang, Q. Wang, T. Zhao, H. Gong, Enhanced X and Ku band microwave absorption powered by a magnetic–dielectric synergistic effect in Pr-doped M/W composite hexaferrites, *J. Mater. Chem. C* 12 (2024) 10513–10531. https://doi.org/10.1039/D4TC01060D.

[13] J. Singh, C. Singh, D. Kaur, S. Bindra Narang, R. Jotania, R. Joshi, Investigation on structural and microwave absorption property of Co^{2+} and Y^{3+} substituted M-type Ba-Sr hexagonal ferrites prepared by a ceramic method, *J. Alloys Compd*. 695 (2017) 792–798. https://doi.org/10.1016/j.jallcom.2016.09.251.

[14] X. Jing, Z. Chen, Q. Zhao, Z. Li, X. Xiong, X. Yang, Q. Wang, H. Huang, H. Jiang, T. Zhao,

H. Gong, Praseodymium dysprosium co-doped M-type strontium ferrite: Intentionally manufacturing heterophase growth to improve microwave absorption performance, *Mater. Today Chem*. 39 (2024) 102151. https://doi.org/10.1016/j.mtchem.2024.102151.

[15] J. Singh, C. Singh, D. Kaur, S.B. Narang, R. Joshi, S.R. Mishra, R. Jotania, M. Ghimire, C.C. Chauhan, Tunable microwave absorption in Co Al substituted M-type Ba Sr hexagonal ferrite, *Mater. Des*. 110 (2016) 749–761. https://doi.org/10.1016/j.matdes.2016.08.049.

[16] W. Chen, W. Wu, M. Li, C. Zhou, S. Zhou, Al^{3+} doped M-type hexagonal Ba–Co ferrites synthesized via ball-milling assisted ceramic process: magnetism and its correlation with structural properties, *J. Mater. Sci. Mater. Electron*. 29 (2018) 8020–8030. https://doi.org/10.1007/s10854-018-8808-7.

[17] J. Li, Y. Hong, S. He, W. Li, H. Bai, Y. Xia, G. Sun, Z. Zhou, A neutron diffraction investigation of high valent doped barium ferrite with wideband tunable microwave absorption, (n.d.).

[18] H. Wei, Z. Huang, J. Cui, P. Zhang, S. Ma, W. Sun, X. Liang, Y. Zhang, Y. Wu, Tailoring electromagnetic wave absorption properties of M-type barium ferrite through Nd^{3+}–(Nb^{5+}/Ta^{5+}) cosubstitution, *Mater. Today Commun*. 39 (2024) 109378. https://doi.org/10.1016/j.mtcomm.2024.109378.

[19] Y. Yang, X. Liu, S. Feng, X. Kan, Q. Lv, Y. Zhao, K.M. Batoo, S.F. Adil, C. Singh, Effects of Pr-Al co-substitution on the magnetic and structural properties of M-type Ca-Sr hexaferrites, *Chin. J. Phys*. 63 (2020) 337–347. https://doi.org/10.1016/j.cjph.2019.11.026.

[20] J. Mohammed, T.T.C. Trudel, H.Y. Hafeez, D. Basandrai, G.R. Bhadu, S.K. Godara, S.B. Narang, A.K. Srivastava, Design of nano-sized Pr^{3+}–Co^{2+}-substituted M-type strontium hexaferrites for optical sensing and electromagnetic interference (EMI) shielding in Ku band, *Appl. Phys. A* 125 (2019) 251. https://doi.org/10.1007/s00339-019-2545-5.

[21] M.A.P. Buzinaro, N.S. Ferreira, F. Cunha, M.A. Macêdo, Hopkinson effect, structural and magnetic properties of M-type Sm^{3+}-doped $SrFe_{12}O_{19}$ nanoparticles produced by a proteic sol–gel process, *Ceram. Int*. 42 (2016) 5865–5872. https://doi.org/10.1016/j.ceramint.2015.12.130.

[22] J. Lakshmikantha, G. Krishnamurthy, B.M. Nagabhushan, E. Melagiriyappa, Dielectric properties and magnetic behavior OF Gd^{3+} substituted M-type $SrFe_{12}O_{19}$ nanoferrites by auto combustion method using urea and citric acid mixtures as a dual fuel, *J. Solid State Chem*. 315 (2022) 123465. https://doi.org/10.1016/j.jssc.2022.123465.

[23] X. Suo, J. Li, W. Zhang, P. Li, Effect of La^{3+} Substitution on the Structure and Magnetic Properties of M-type Sr Hexaferrites, (n.d.).

[24] Y. Huang, Z. Zhang, W. Xing, T. Xu, D. Zhao, W. Yang, J. Lin, K. Shi, J. Li, Z. Zhou, Enhanced Polarization Loss toward Lanthanum–Samarium Doping-Encoded Defect Genes of Ferrite for Optimizing Microwave Absorption, *ACS Appl. Nano Mater*. 7 (2024) 11146–11158. https://doi.org/10.1021/acsanm.4c00419.

[25] J.-L. Liu, P. Zhang, X.-K. Zhang, Q.-Q. Xie, D.-J. Pan, J. Zhang, M. Zhang, Synthesis and microwave absorbing properties of La-doped Sr-hexaferrite nanopowders via sol–gel auto-combustion method, *Rare Met*. 36 (2017) 704–710. https://doi.org/10.1007/s12598-015-0671-6.

[26] X. Jing, Q. Zhao, Q. Wang, X. Xiong, X. Yang, H. Huang, C. Yuan, J. Yan, G. Tan, T. Zhao, H. Gong, Exploration of the microwave absorption mechanism of rare earth enhanced M-type strontium ferrite: synergistic effect of lattice occupation and impurity phase, *J. Mater. Sci.*

Mater. Electron. 36 (2025) 442. https://doi.org/10.1007/s10854-025-14513-8.

[27] Z. Chen, Bo Xu, Z. Li, N. Zhou, H. Gong, X. Jing, The influence of Ho doping on the morphology and magnetic properties of M-type strontium ferrite with different Fe/Sr, *Mater. Chem. Phys*. 312 (2024) 128635. https://doi.org/10.1016/j.matchemphys.2023.128635.

[28] N. Chen, K. Yang, M. Gu, Microwave absorption properties of La-substituted M-type strontium ferrites, *J. Alloys Compd*. 490 (2010) 609–612. https://doi.org/10.1016/j.jallcom.2009.10.116.

[29] B.K. Rai, S.R. Mishra, V.V. Nguyen, J.P. Liu, Synthesis and characterization of high coercivity rare-earth ion doped $Sr_{0.9}RE_{0.1}Fe_{10}Al_2O_{19}$ (RE: Y, La, Ce, Pr, Nd, Sm, and Gd), *J. Alloys Compd*. 550 (2013) 198–203. https://doi.org/10.1016/j.jallcom.2012.09.021.

[30] J. Xia, W. Chen, W. Wu, X. Wu, S. Zhou, C. Xiao, Structural and Magnetic Properties of La-Substituted M-Type Hexagonal Sr–Ni Ferrites Synthesized by Ball-Milling-Assisted Ceramic Process, *J. Supercond. Nov. Magn*. 32 (2019) 441–449. https://doi.org/10.1007/s10948-018-4739-z.

[31] T.R. Wagner, Preparation and Crystal Structure Analysis of Magnetoplumbite-Type $BaGa_{12}O_{19}$, *J. Solid State Chem*. 136 (1998) 120–124. https://doi.org/10.1006/jssc.1997.7681.

[32] G.A. Alna'washi, A.M. Alsmadi, I. Bsoul, B. Salameh, G.M. Alzoubi, M. Shatnawi, S.M. Hamasha, S.H. Mahmood, Investigation on X-ray photoelectron spectroscopy, structural and low temperature magnetic properties of Ni-Ti co-substituted M-type strontium hexaferrites prepared by ball milling technique, *Results Phys*. 28 (2021) 104574. https://doi.org/10.1016/j.rinp.2021.104574.

[33] E.E. Ateia, O. Rabie, A.T. Mohamed, Multi-susceptible single-phased hexaferrite with significant magnetic switching properties by selectively doping, *Phys. Scr*. 98 (2023) 065801. https://doi.org/10.1088/1402-4896/acd230.

[34] T.J. Frankcombe, Y. Liu, Interpretation of Oxygen 1s X-ray Photoelectron Spectroscopy of ZnO, *Chem. Mater*. 35 (2023) 5468–5474. https://doi.org/10.1021/acs.chemmater.3c00801.

[35] K. Shehzad, M. Ahmad, S. Al-Sulaimi, M. Alam, X. Chen, W. Xu, J.-H. Liu, Facile synthesis of novel hexagonal strontium ferrites for promising adsorption of cadmium from aqueous solutions, *Mater. Chem. Phys*. 318 (2024) 129222. https://doi.org/10.1016/j.matchemphys.2024.129222.

[36] X. Yang, Z. Chen, D. Zhou, X. Xiong, X. Jing, T. Zhao, H. Gong, B. Shen, Effect of the interaction of Fe- and Ce-contents on the structure and magnetic properties of M-type strontium ferrites, *Ceram. Int*. 50 (2024) 32465–32476. https://doi.org/10.1016/j.ceramint.2024.06.055.

[37] C.-C. Huang, A.-H. Jiang, C.-H. Liou, Y.-C. Wang, C.-P. Lee, T.-Y. Hung, C.-C. Shaw, Y.-H. Hung, M.-F. Kuo, C.-H. Cheng, Magnetic property enhancement of cobalt-free M-type strontium hexagonal ferrites by $CaCO_3$ and SiO_2 addition, *Intermetallics* 89 (2017) 111–117. https://doi.org/10.1016/j.intermet.2017.06.001.

[38] M. Küpferling, R. Grössinger, M.W. Pieper, G. Wiesinger, H. Michor, C. Ritter, F. Kubel, Structural phase transition and magnetic anisotropy of La-substituted M -type Sr hexaferrite, *Phys. Rev. B* 73 (2006) 144408. https://doi.org/10.1103/PhysRevB.73.144408.

[39] M. Green, X. Chen, Recent progress of nanomaterials for microwave absorption, *J. Materiomics* 5 (2019) 503–541. https://doi.org/10.1016/j.jmat.2019.07.003.

[40] S. Shao, S. Xing, K. Bi, T. Zhao, H. Wang, Y. Tang, J. Liu, F. Wang, Fabrication of graphene/polyimide/Co-N-C aerogel with reinforced electromagnetic losses and broadband absorption for highly efficient microwave absorption and thermal insulation, Chem. Eng. J. 494

View Article Online
DOI: 10.1039/D5TC02015H

(2024) 152976. https://doi.org/10.1016/j.cej.2024.152976.

[41] S. Shao, C. Guo, H. Wang, S. Wang, T. Zhao, Y. Tang, J. Liu, F. Wang, Multifunctional graphene/Ti3C2T MXene aerogel inlaid with Ni@TiO2 core-shell microspheres for high-efficiency electromagnetic wave absorption and thermal insulation, Chem. Eng. J. 488 (2024) 150918. https://doi.org/10.1016/j.cej.2024.150918.

[42] X. Wang, B. Wang, S. Wei, Y. Wang, Y. Liang, L. Li, Tunable magnetic and microwave absorption properties of barium ferrite particles by site-selective Co^{2+}-Zr^{4+} Co-doping, *J. Alloys Compd*. 960 (2023) 170777. https://doi.org/10.1016/j.jallcom.2023.170777.

[43] J. Gao, Z. Ma, F. Liu, X. Weng, K. Meng, Preparation and microwave absorption properties of Gd–Co ferrite@silica@carbon multilayer core–shell structure composites, *Chem. Eng. J*. 446 (2022) 137157. https://doi.org/10.1016/j.cej.2022.137157.

[44] H. Kaur, A. Marwaha, C. Singh, S.B. Narang, R. Jotania, S. Jacobo, A.S.B. Sombra, S.V. Trukhanov, A.V. Trukhanov, P. Dhruv, Investigation of structural, hysteresis and electromagnetic parameters for microwave absorption application in doped Ba–Sr hexagonal ferrites at X-band, *J. Alloys Compd*. 806 (2019) 1220–1229. https://doi.org/10.1016/j.jallcom.2019.07.032.

[45] M.N. Ashiq, R.B. Qureshi, M.A. Malana, M.F. Ehsan, Fabrication, structural, dielectric and magnetic properties of tantalum and potassium doped M-type strontium calcium hexaferrites, *J. Alloys Compd*. 651 (2015) 266–272. https://doi.org/10.1016/j.jallcom.2015.05.181.

[46] J. Song, Y. Gao, G. Tan, Q. Man, Z. Wang, Comparative study of microwave absorption properties of Ni–Zn ferrites obtained from different synthesis technologies, *Ceram. Int*. 48 (2022) 22896–22905. https://doi.org/10.1016/j.ceramint.2022.04.237.

[47] N.N. Ali, Y. Atassi, A. Salloum, A. Charba, A. Malki, M. Jafarian, Comparative study of microwave absorption characteristics of (Polyaniline/NiZn ferrite) nanocomposites with different ferrite percentages, *Mater. Chem. Phys*. 211 (2018) 79–87. https://doi.org/10.1016/j.matchemphys.2018.02.017.

[48] C. Guo, S. Shao, X. Zhang, Y. Tang, L. Wang, J. Liu, L. Wu, K. Bi, F. Wang, Multifunctional MXene/rGO aerogels loaded with Co/MnO nanocomposites for enhanced electromagnetic wave absorption, thermal insulation and pressure sensing, Nano Res. 17 (2024) 7803–7813. https://doi.org/10.1007/s12274-024-6840-x.

[49] M. Green, L. Tian, P. Xiang, J. Murowchick, X. Tan, X. Chen, Co2P nanoparticles for microwave absorption, *Mater. Today Nano* 1 (2018) 1–7. https://doi.org/10.1016/j.mtnano.2018.04.004.

[50] Y. Tang, S. Shao, C. Guo, K. Bi, H. Wang, T. Zhao, J. Liu, F. Wang, Multifunctional ultralight magnetic Fe3O4@SiO2/Ti3C2T /rGO aerogel with efficient electromagnetic wave absorption and thermal management properties, Carbon 228 (2024) 119314. https://doi.org/10.1016/j.carbon.2024.119314.

[51] S. Ghosh, S. Sharma, W. Li, A. Nozariasbmarz, L. Raman, N. Liu, G.K. Goyal, Y. Zhang, S.E. Perini, M. Lanagan, S. Priya, B. Poudel, Broadband and Tunable Microwave Absorption Properties from Large Magnetic Loss in Ni–Zn Ferrite, *Adv. Mater. Technol*. 9 (2024) 2301857. https://doi.org/10.1002/admt.202301857.

View Article Online
DOI: 10.1039/D5TC02015H

Data availability statement

All relevant data are within the paper.